A Step-Superposition-Based Analysis Approach to Modeling Resonant Converters

Jie Lu, *Member, IEEE*, Ashish Kumar, *Student Member, IEEE*, and Khurram K. Afridi, *Senior Member, IEEE*

***Abstract*—This paper introduces a new analysis approach to modeling resonant converters that can be used to determine closed-form expressions for the exact resonant network waveforms. This approach, based on superposition of step responses to inverter and rectifier imposed steps, can easily be applied to resonant converters with high-order resonant networks, multiple inverters, and/or rectifiers. The usefulness of the proposed analysis approach is demonstrated first by applying it to a series-resonant converter, wherein it is used to determine accurate closed-form expressions for its tank current in different operating modes. These expressions are utilized to draw insights that help identify the converter's operating mode, and determine associated expressions for its output voltage and the switching frequency required to achieve a desired output power. The proposed approach is also applied to the multi-inverter multi-element impedance control network (ICN) resonant converter, wherein it is used to derive closed-form expressions for the converter's currents. These expressions are utilized to evaluate the behavior and optimize the design of an ICN resonant converter. A prototype 200-W 500-kHz ICN resonant converter optimized using the proposed approach is used to validate the modeling results. It is shown that there is an excellent agreement between the experimental and modeled waveforms during steady-state operation as well as during startup transients.**

***Index Terms*—High-order resonant network, impedance control network (ICN), resonant converter, startup transient modeling, steady-state modeling, step superposition (S2).**

I. INTRODUCTION

RESONANT converters are typically analyzed and designed using fundamental-frequency analysis [1]–[3], wherein network waveforms are approximated by their fundamental components and switching frequency harmonics are neglected. This modeling method simplifies the design of resonant converters as it converts the nonlinear power converter into an approximately equivalent linear circuit. However, this approach becomes inaccurate when the converter tank waveforms are significantly nonsinusoidal, as is often the case when the quality factor (Q) of the resonant network is low. More accurate modeling approaches that consider higher order harmonics in the resonant network waveforms have also been proposed [4]; however, these approaches are limited in their accuracy by the number of harmonics considered, and become analytically intractable and computationally intensive when a large number of harmonics are included. There are two related general approaches for exact analysis of resonant converters: state-space analysis and state-plane analysis. State-space analysis identifies the operating modes of a resonant converter over one switching cycle, and solves the state vectors recursively from one mode to the next [5]–[12]. State-space analysis is an accurate and general approach to the analysis of resonant converters, but it requires complicated and time-consuming matrix computations. On the other hand, state-plane analysis converts the time-domain analysis of resonant converters to geometrical analysis, where tank waveforms are described using segments of circles, lines, or ellipses [13]–[22]. Through such graphical representations, state-plane analysis simplifies the exact analysis of complicated resonant tank behavior. However, its application is practically limited to simple resonant converters (e.g., with up to two or three tank elements). To analyze high-order resonant converters with multiple tank elements, this method needs to employ complicated higher dimensional or multiple 2-D state planes [20], and becomes difficult to use. Furthermore, both of the aforementioned exact modeling approaches require finding all the operating modes of the resonant converter, which is not straightforward particularly for high-order resonant converter topologies with multiple inverters and/or rectifiers [23]–[38]. Therefore, there is a need for an exact yet general and easily applicable method for modeling topologically advanced high-order resonant converters.

This paper introduces a new analysis approach to modeling resonant converters that can be used to determine closed-form expressions for the exact resonant network waveforms. This approach, based on superposition of step responses to inverter and rectifier imposed steps, can easily be applied to resonant converters with high-order resonant networks, multiple inverters, and/or rectifiers. The usefulness of the proposed analysis approach is demonstrated first by applying it to a series-resonant converter (SRC), wherein it is used to determine accurate closed-form expressions for its tank current in different operating modes. These expressions are utilized to draw insights that help identify the converter's operating mode, and determine associated expressions for its output voltage and the switching frequency required to achieve a desired output power. The proposed approach is also applied to the multi-inverter multi-element impedance control

---

Manuscript received May 23, 2017; revised August 10, 2017; accepted September 19, 2017. Date of publication September 25, 2017; date of current version April 20, 2018. This work was supported by the National Science Foundation under Award 1307699. Recommended for publication by Associate Editor H. H.-C. Iu. *(Corresponding author: Ashish Kumar.)*

J. Lu is with FINsix Corporation, Menlo Park, CA USA (e-mail: jie.lu@colorado.edu).

A. Kumar and K. K. Afridi are with the Department of Electrical, Computer, and Energy Engineering, University of Colorado Boulder, Boulder, CO 80309 USA (e-mail: ashish.kumar@colorado.edu; khurram.afridi@colorado.edu).

Color versions of one or more of the figures in this paper are available online at http://ieeexplore.ieee.org.

Digital Object Identifier 10.1109/TPEL.2017.2756873

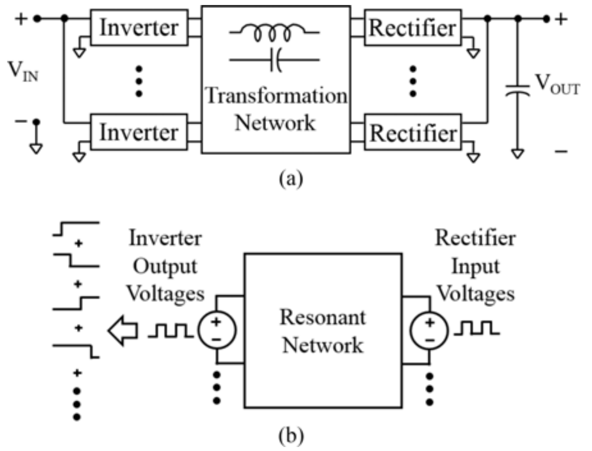

Fig. 1. Voltage-fed voltage-loaded dc–dc resonant converter: (a) General architecture and (b) proposed analysis method using a S2 model. In the proposed approach, the inverter output voltages and rectifier input voltages are modeled as rectangular-wave sources, which are further modeled as series of time-shifted positive and negative steps.

network (ICN) resonant converter [31]–[38], wherein it is used to derive closed-form expressions for the converter's currents. These expressions are utilized to evaluate the behavior and optimize the design of an ICN resonant converter. The modeling results are validated using a 200-W 500-kHz ICN resonant converter optimized using the proposed approach. It is shown that there is an excellent agreement between the experimental and modeled waveforms during steady-state operation and during startup transients. This study expands on an earlier paper [39] through additional modeling results, analysis, and discussion.

The remainder of this paper is organized as follows: Section II describes the proposed step-superposition (S2) analysis approach. Section III applies the S2 analysis to an SRC. The class of converters to which S2 analysis is applicable is identified in Section IV. Section V applies S2 analysis to an ICN resonant converter. Finally, the conclusions of the paper are summarized in Section VI.

II. STEP-SUPERPOSITION (S2) ANALYSIS

The general architecture of a voltage-fed voltage-loaded dc–dc resonant converter is shown in Fig. 1(a). This architecture comprises an inversion stage with one or more inverters, a transformation stage with a resonant network, and a rectification stage with one or more rectifiers. In the proposed analysis approach, the inverter output voltages and rectifier input voltages are modeled as rectangular-wave sources, as shown in Fig. 1(b). The response of the resonant network is obtained for each source, with the other sources set to zero. To compute this single-source response, the rectangular-wave source is further decomposed into a sum of time-shifted positive and negative steps. The tank response to each step is obtained and summed to get the full single-source response. Finally, all the single-source responses are superposed to obtain the complete response of the resonant network in the presence of all inverter and rectifier sources. Note that the summation of steps and superposition of responses are performed under the implicit assumption that the resonant network is linear time invariant (LTI). In view of the salient features of this approach as described above, it is termed as step-superposition (S2) analysis. While explained here in the context of a voltage-fed voltage-loaded resonant converter architecture, S2 analysis is applicable to a broader range of converter architectures, including current-fed and/or current-loaded converters.

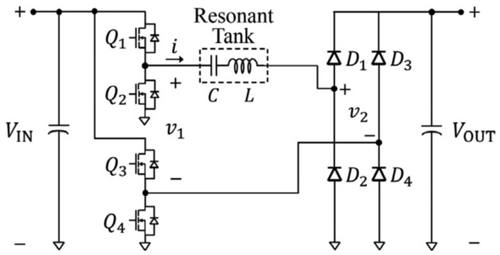

Fig. 2. Full-bridge SRC. V_{IN} is the input voltage and V_{OUT} is the output voltage.

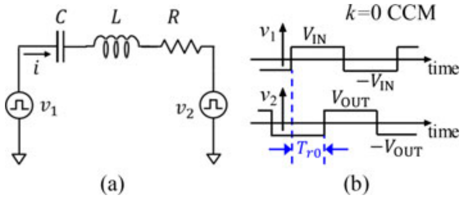

Fig. 3. (a) Equivalent model of the full-bridge SRC of Fig. 2 and (b) waveforms of the inverter output voltage v_1 and rectifier input voltage v_2 when the converter operates in the $k = 0$ CCM mode.

III. APPLICATION TO SRC

To better understand the S2 analysis approach, the simple example of a full-bridge SRC is considered. The converter topology is shown in Fig. 2. The SRC can operate in different modes: an above-resonance mode and several below-resonance modes. In this section, S2 analysis is applied to two example modes of the SRC to demonstrate its usefulness.

A. SRC Operating in Above-Resonance Mode

In this section, the SRC of Fig. 2 is assumed to be switching at a frequency higher than the resonant frequency of the series-resonant tank (that is, according to the terminology defined in [40], the $k = 0$ continuous-conduction mode (CCM)), with the inverter transistors operating at 50% duty ratio. Fig. 3(a) shows the equivalent model for the converter of Fig. 2 with the two voltages imposed on the resonant network—the inverter output voltage v_1 and the rectifier input voltage v_2 of Fig. 2—modeled by square-wave sources. The resistor R in Fig. 3(a) models the losses associated with the inverter and rectifier transistors, the inductor, and the capacitor. The inverter output and rectifier input voltages (v_1 and v_2) of the SRC are plotted in Fig. 3(b). As can be seen, the rectifier input voltage v_2 lags the inverter output voltage v_1 by time T_{r0}. This time lag arises when the SRC operates in the above-resonance mode, in which the resonant tank current i lags the inverter output voltage v_1. Since the rectifier switches commutate at the zero crossings of the tank current, the rectifier input voltage v_2 also lags the inverter output voltage v_1 by the same amount. The inverter input and rectifier output voltages can be decomposed into a sum of time-shifted positive and negative steps, as given in (1) and (2) shown at the bottom of this page. Here, $V_{1,\text{ini}}$ is the voltage at the output of the inverter and $V_{2,\text{ini}}$ is the voltage at the input of the rectifier before the converter is turned on, time t is taken to be zero when the converter is turned on, T_s is the switching period of the converter, $K(= 1, 2, 3\ldots)$ is the number of the switching cycle of interest (the Kth switching cycle), and t'_K is the time elapsed within the switching cycle of interest. The relationship between t, t'_K, and K is given by

$$t'_K = t - (K - 1)\,T_s. \tag{3}$$

Under the condition that the resonant tank of the SRC is lightly damped, that is, $R < 2\sqrt{\frac{L}{C}}$, which is typically true for a highly efficient converter, the response of the resonant tank current to a step in the inverter output or rectifier input voltage is given by

$$i_{\text{step}}(t) = \frac{V_x}{\omega_d L} e^{-\alpha t} \sin \omega_d t \tag{4}$$

where $\alpha = \frac{R}{2L}$, $\omega_d = \sqrt{\frac{1}{LC} - (\frac{R}{2L})^2}$, and V_x is the magnitude of the voltage step, which equals $2V_{\text{IN}}$ when the step is in the inverter output voltage, and $2V_{\text{OUT}}$ when the step is in the rectifier input voltage. Each step in the inverter output voltage v_1 and rectifier input voltage v_2 given in (1) and (2) excites a response in the tank current of the form given in (4). The components i_1 and i_2 of the tank current i generated by the two voltage sources v_1 and v_2, respectively, can be obtained by adding these individual step responses, as given in (5) and (6) shown at the bottom of this page. The summations in (5) and (6) can be simplified using Euler's identity, trigonometric identities, and geometric series analysis, as described in Appendix A, to yield a closed-form expression for the steady-state tank current $i(t) = i_1(t) + i_2(t)$, where

$$i_1(t) = \begin{cases} \frac{V_{\text{IN}}}{\omega_d L} \frac{\sin\left(\omega_d t'_K - \frac{1}{4}\omega_d T_s\right)}{2\cos\left(\frac{\omega_d T_s}{4}\right)}, & 0 \le t'_K < \frac{T_s}{2} \\ \frac{V_{\text{IN}}}{\omega_d L} \frac{\sin\left(\frac{3}{4}\omega_d T_s - \omega_d t'_K\right)}{2\cos\left(\frac{\omega_d T_s}{4}\right)}, & \frac{T_s}{2} \le t'_K < T_s \end{cases} \tag{7}$$

$$i_2(t) = \begin{cases} -\frac{V_{\text{OUT}}}{\omega_d L} \frac{\sin\left(-\omega_d t'_K - \frac{1}{4}\omega_d T_s + \omega_d T_{r0}\right)}{2\cos\left(\frac{\omega_d T_s}{4}\right)}, & 0 \le t'_K < T_{r0} \\ -\frac{V_{\text{OUT}}}{\omega_d L} \frac{\sin\left(\omega_d t'_K - \frac{1}{4}\omega_d T_s - \omega_d T_{r0}\right)}{2\cos\left(\frac{\omega_d T_s}{4}\right)}, & T_{r0} \le t'_K < T_{r0} + \frac{T_s}{2} \\ -\frac{V_{\text{OUT}}}{\omega_d L} \frac{\sin\left(-\omega_d t'_K + \frac{3}{4}\omega_d T_s + \omega_d T_{r0}\right)}{2\cos\left(\frac{\omega_d T_s}{4}\right)}, & T_{r0} + \frac{T_s}{2} \le t'_K < T_s \end{cases}. \tag{8}$$

$$v_1(t) = \begin{cases} V_{1,\text{ini}} - \left(V_{\text{IN}} + V_{1,\text{ini}}\right) u(t) + \sum_{m=0}^{K-1} 2V_{\text{IN}} u\left(t'_K + mT_s\right) \\ \quad - \sum_{m=1}^{K-1} 2V_{\text{IN}} u\left(t'_K - \frac{T_s}{2} + mT_s\right), & 0 \le t'_K < \frac{T_s}{2} \\ V_{1,\text{ini}} - \left(V_{\text{IN}} + V_{1,\text{ini}}\right) u(t) + \sum_{m=0}^{K-1} 2V_{\text{IN}} u\left(t'_K + mT_s\right) \\ \quad - \sum_{m=0}^{K-1} 2V_{\text{IN}} u\left(t'_K - \frac{T_s}{2} + mT_s\right), & \frac{T_s}{2} \le t'_K < T_s \end{cases} \tag{1}$$

$$v_2(t) = \begin{cases} V_{2,\text{ini}} - \left(V_{\text{OUT}} + V_{2,\text{ini}}\right) u(t - T_{r0}) + \sum_{m=1}^{K-1} 2V_{\text{OUT}} u\left(t'_K - T_{r0} + mT_s\right) \\ \quad - \sum_{m=1}^{K-1} 2V_{\text{OUT}} u\left(t'_K - T_{r0} - \frac{T_s}{2} + mT_s\right), & 0 \le t'_K < T_{r0} \\ V_{2,\text{ini}} - \left(V_{\text{OUT}} + V_{2,\text{ini}}\right) u(t - T_{r0}) + \sum_{m=0}^{K-1} 2V_{\text{OUT}} u\left(t'_K - T_{r0} + mT_s\right) \\ \quad - \sum_{m=1}^{K-1} 2V_{\text{OUT}} u\left(t'_K - T_{r0} - \frac{T_s}{2} + mT_s\right), & T_{r0} \le t'_K < T_{r0} + \frac{T_s}{2} \\ V_{2,\text{ini}} - \left(V_{\text{OUT}} + V_{2,\text{ini}}\right) u(t - T_{r0}) + \sum_{m=0}^{K-1} 2V_{\text{OUT}} u\left(t'_K - T_{r0} + mT_s\right) \\ \quad - \sum_{m=0}^{K-1} 2V_{\text{OUT}} u\left(t'_K - T_{r0} - \frac{T_s}{2} + mT_s\right), & T_{r0} + \frac{T_s}{2} \le t'_K < T_s \end{cases} \tag{2}$$

$$i_1(t) = \begin{cases} -\frac{\left(V_{\text{IN}} + V_{1,\text{ini}}\right)}{2V_{\text{IN}}} i_{\text{step}}(t) + \sum_{m=0}^{K-1} i_{\text{step}}\left(t'_K + mT_s\right) \\ \quad - \sum_{m=1}^{K-1} i_{\text{step}}\left(t'_K - \frac{T_s}{2} + mT_s\right), & 0 \le t'_K < \frac{T_s}{2} \\ -\frac{\left(V_{\text{IN}} + V_{1,\text{ini}}\right)}{2V_{\text{IN}}} i_{\text{step}}(t) + \sum_{m=0}^{K-1} i_{\text{step}}\left(t'_K + mT_s\right) \\ \quad - \sum_{m=0}^{K-1} i_{\text{step}}\left(t'_K - \frac{T_s}{2} + mT_s\right), & \frac{T_s}{2} \le t'_K < T_s \end{cases} \tag{5}$$

$$i_2(t) = \begin{cases} \frac{\left(V_{\text{OUT}} + V_{2,\text{ini}}\right)}{2V_{\text{OUT}}} i_{\text{step}}(t - T_{r0}) - \sum_{m=1}^{K-1} i_{\text{step}}\left(t'_K - T_{r0} + mT_s\right) \\ \quad + \sum_{m=1}^{K-1} i_{\text{step}}\left(t'_K - T_{r0} - \frac{T_s}{2} + mT_s\right), & 0 \le t'_K < T_{r0} \\ \frac{\left(V_{\text{OUT}} + V_{2,\text{ini}}\right)}{2V_{\text{OUT}}} i_{\text{step}}(t - T_{r0}) - \sum_{m=0}^{K-1} i_{\text{step}}\left(t'_K - T_{r0} + mT_s\right) \\ \quad + \sum_{m=1}^{K-1} i_{\text{step}}\left(t'_K - T_{r0} - \frac{T_s}{2} + mT_s\right), & T_{r0} \le t'_K < T_{r0} + \frac{T_s}{2} \\ \frac{\left(V_{\text{OUT}} + V_{2,\text{ini}}\right)}{2V_{\text{OUT}}} i_{\text{step}}(t - T_{r0}) - \sum_{m=0}^{K-1} i_{\text{step}}\left(t'_K - T_{r0} + mT_s\right) \\ \quad + \sum_{m=0}^{K-1} i_{\text{step}}\left(t'_K - T_{r0} - \frac{T_s}{2} + mT_s\right), & T_{r0} + \frac{T_s}{2} \le t'_K < T_s \end{cases}. \tag{6}$$

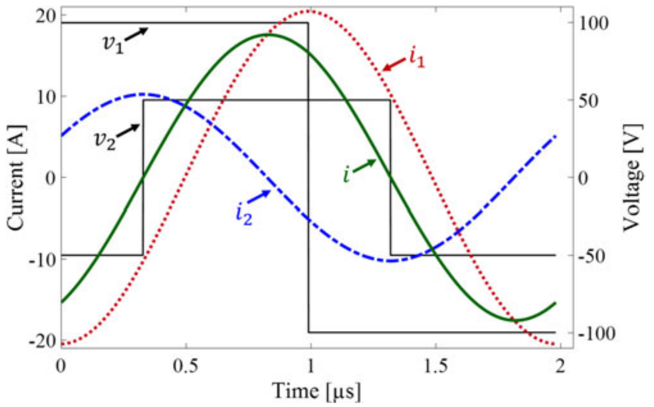

Fig. 4. S2-modeled tank current waveform of the SRC $i(t)$ and its two components $i_1(t)$ and $i_2(t)$, with the converter operating in steady state in the above-resonance mode ($k = 0$ CCM) at 100-V input voltage and 50-V output voltage. The values of the tank components are $L = 100\ \mu$H and $C = 1.0132$ nF. The tank resonant frequency is 500 kHz and the switching frequency is 505 kHz.

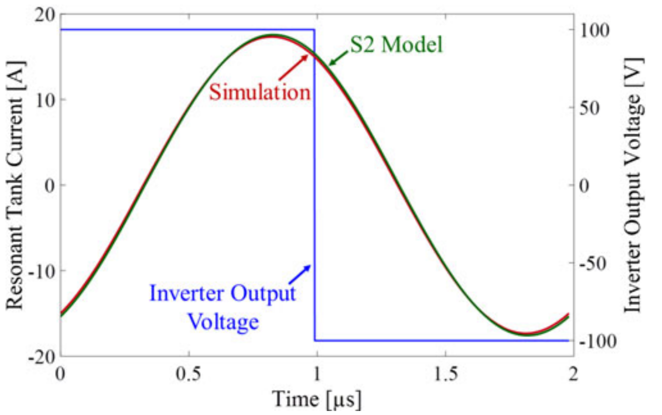

Fig. 5. Comparison of S2-modeled and LTSpice-simulated steady-state tank current waveforms of the SRC operating in the above-resonance mode ($k = 0$ CCM) with the same input and output voltages, component values, and switching frequency as in Fig. 4.

Since the initial step responses at the beginning of the converter's operation die out in steady state, (7) and (8) are independent of initial voltages.

The time lag of the rectifier (T_{r0}) can be obtained using the fact that at the time instant $t'_K = T_{r0}$, the rectifier switches commutate and the tank current is zero. Solving (7) and (8) under the condition that the tank current $i(t) = i_1(t) + i_2(t) = 0$, the rectifier time lag T_{r0} can be expressed as

$$T_{r0} = \frac{\arcsin\left(-\frac{V_{\mathrm{OUT}}}{V_{\mathrm{IN}}}\sin\left(\frac{\omega_d T_s}{4}\right)\right) + \frac{\omega_d T_s}{4}}{\omega_d} \tag{9}$$

The above application of S2 analysis pertains to the steady-state operation of the SRC. However, S2 analysis is a general method that can be used to compute the startup transients of a converter as well, as will be shown in Section V.

The SRC of Fig. 2 is evaluated using S2 analysis for an input voltage of 100 V, an output voltage of 50 V, an inductance $L = 100\ \mu$H, and a capacitance $C = 1.0132$ nF, resulting in a resonant frequency of 500 kHz. The inverter transistors are switched at a frequency slightly higher than the resonant frequency, at 505 kHz. The S2-modeled steady-state tank current i in this above-resonance mode and its two components i_1 and i_2 as given by (7) and (8) are shown in Fig. 4. As can be seen, the component i_1 of the tank current lags the inverter output voltage v_1 by approximately 90°. This is because i_1 is determined by setting the rectifier input voltage v_2 to zero. Under this condition, the inverter is loaded only by the series-resonant tank, whose impedance when operating above resonance is almost purely inductive (with a small resistive component due to losses). A similar analysis can be used to show that the component i_2 of the tank current leads the rectifier input voltage v_2 by nearly 90° in the above-resonance mode, as also evident in Fig. 4. The S2-modeled tank current i is also compared with simulations performed in LTSpice. The modeled and simulated tank current waveforms are shown in Fig. 5. As can be seen, the modeled tank current matches its simulated counterpart to a high degree of accuracy.

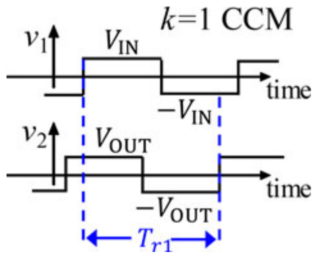

Fig. 6. Waveforms of the inverter output voltage v_1 and rectifier input voltage v_2 of the SRC of Fig. 2 when the converter operates in the $k = 1$ CCM mode.

B. SRC Operating in Below-Resonance Mode

In this section, S2 analysis is applied to the SRC of Fig. 2 operating in a below-resonance mode. Without loss of generality, we consider the most commonly used below-resonance mode: the $k = 1$ CCM mode, where the switching frequency f_s is lower than the resonant frequency f_0, but higher than $f_0/2$ [40]. The inverter output voltage v_1 and rectifier input voltage v_2 in this below-resonance mode of the SRC are plotted in Fig. 6. In this mode, the resonant tank current leads the inverter output voltage; therefore, the rectifier input voltage also leads the inverter output voltage, which is equivalently represented by a time lag T_{r1} larger than half the switching period $T_s/2$ in Fig. 6. The inverter output voltage v_1 in this below-resonance mode is the same as that in the above-resonance mode, and is given by (1). The rectifier input voltage v_2 in the below-resonance mode now has a time shift of T_{r1} with respect to the inverter output voltage, and is given by (10) shown at the bottom of the next page. The component i_1 of the tank current resulting from the inverter output voltage v_1 in the below-resonance mode also remains the same as in the above-resonance mode, and is given by (5) and (7). The component i_2 of the tank current resulting from the rectifier input voltage v_2 in the below-resonance mode is given by (11) shown at the bottom of the next page. Using the simplification approach given in Appendix A, the component i_2 of the tank current in steady state can be expressed as

$$i_2(t) = \begin{cases} -\frac{V_{\mathrm{OUT}}}{\omega_d L}\frac{\sin\left(\omega_d t'_K+\frac{3}{4}\omega_d T_s-\omega_d T_{r1}\right)}{2\cos\left(\frac{\omega_d T_s}{4}\right)}, & 0 \le t'_K < T_{r1}-\frac{T_s}{2} \\ -\frac{V_{\mathrm{OUT}}}{\omega_d L}\frac{\sin\left(-\omega_d t'_K-\frac{1}{4}\omega_d T_s+\omega_d T_{r1}\right)}{2\cos\left(\frac{\omega_d T_s}{4}\right)}, & T_{r1}-\frac{T_s}{2} \le t'_K < T_{r1} \\ -\frac{V_{\mathrm{OUT}}}{\omega_d L}\frac{\sin\left(\omega_d t'_K-\frac{1}{4}\omega_d T_s-\omega_d T_{r1}\right)}{2\cos\left(\frac{\omega_d T_s}{4}\right)}, & T_{r1} \le t'_K < T_s \end{cases}. \quad (12)$$

Again, the complete tank current is given by $i(t) = i_1(t) + i_2(t)$. Since the tank current is zero at the rectifier commutation instant ($t'_K = T_{r1}$), the time lag T_{r1} of the rectifier input voltage in the below-resonance mode can be found using (7) and (12) by applying the condition that $i(t) = i_1(t) + i_2(t) = 0$, and is given by

$$T_{r1} = \frac{\arcsin\left(\frac{V_{\mathrm{OUT}}}{V_{\mathrm{IN}}}\sin\left(\frac{\omega_d T_s}{4}\right)\right)+\frac{3\omega_d T_s}{4}}{\omega_d}. \quad (13)$$

The S2-modeled steady-state tank current of the SRC of Fig. 2, $i(t)$, and its two components $i_1(t)$ and $i_2(t)$ as given by (7) and (12), when operating in the below-resonance mode with the same input voltage, output voltage, and tank component values as those considered in the above-resonance mode, but with the switching frequency now reduced below resonance to 490 kHz, are shown in Fig. 7. As can be seen, in this below-resonance mode, the component i_1 of the tank current leads the inverter output voltage v_1 by nearly 90°. Similar to the discussion for the above-resonance mode, this phase relationship between i_1 and v_1 in the below-resonance mode arises because, with v_2 set to zero, the inverter is loaded only by the series-resonant tank, whose impedance when operating below resonance is almost purely capacitive. A similar analysis shows that the component i_2 of the tank current lags the rectifier input voltage v_2 by approximately 90° in the below-resonance mode, as also shown in Fig. 7. The S2-modeled tank current waveform is also compared with its LTSpice-simulated counterpart, as shown in Fig. 8. It can be seen that the S2-modeled waveform matches the simulated waveform to a high degree of accuracy in this below-resonance mode as well.

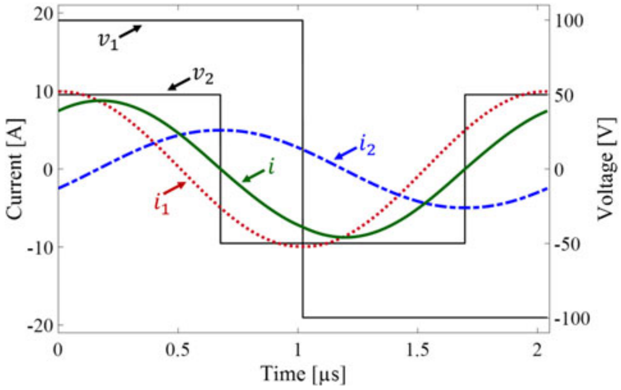

Fig. 7. S2-modeled steady-state tank current waveform of the SRC $i(t)$ and its two components $i_1(t)$ and $i_2(t)$, while operating in a below-resonance mode ($k = 1$ CCM) with 100-V input voltage and 50-V output voltage. The values of the tank components are $L = 100$ μH and $C = 1.0132$ nF. The tank resonant frequency is 500 kHz and the switching frequency is 490 kHz.

C. Identification of the Operating Mode of the SRC

S2 analysis can also be used to easily identify the operating mode of the SRC. To do so, the tank current expressions obtained from S2 analysis are used to derive the output power of the converter. Assuming lossless power conversion, the output power can be obtained by averaging the instantaneous output power of the inverter over one switching period, as

$$P_{\mathrm{OUT}} = \frac{1}{T_s}\int_0^{T_s} v_1(t)\, i(t)\, dt = \frac{2}{T_s}V_{\mathrm{IN}}\int_0^{\frac{T_s}{2}} i(t)\, dt. \quad (14)$$

Here, the first integral over the switching period T_s is converted to the second integral over half the switching period $T_s/2$, using the fact that both the inverter output voltage and the

$$v_2(t) = \begin{cases} V_{2,\mathrm{ini}} - \left(V_{\mathrm{OUT}}+V_{2,\mathrm{ini}}\right)u\left(t-T_{r1}\right) + \sum_{m=1}^{K-1} 2V_{\mathrm{OUT}}u\left(t'_K - T_{r1} + mT_s\right) \\ \qquad -\sum_{m=1}^{K-1} 2V_{\mathrm{OUT}}u\left(t'_K - T_{r1} + \frac{T_s}{2} + mT_s\right), & 0 \le t'_K < T_{r1}-\frac{T_s}{2} \\ V_{2,\mathrm{ini}} - \left(V_{\mathrm{OUT}}+V_{2,\mathrm{ini}}\right)u\left(t-T_{r1}\right) + \sum_{m=1}^{K-1} 2V_{\mathrm{OUT}}u\left(t'_K - T_{r1} + mT_s\right) \\ \qquad -\sum_{m=0}^{K-1} 2V_{\mathrm{OUT}}u\left(t'_K - T_{r1} + \frac{T_s}{2} + mT_s\right), & T_{r1}-\frac{T_s}{2} \le t'_K < T_{r1} \\ V_{2,\mathrm{ini}} - \left(V_{\mathrm{OUT}}+V_{2,\mathrm{ini}}\right)u\left(t-T_{r1}\right) + \sum_{m=0}^{K-1} 2V_{\mathrm{OUT}}u\left(t'_K - T_{r1} + mT_s\right) \\ \qquad -\sum_{m=0}^{K-1} 2V_{\mathrm{OUT}}u\left(t'_K - T_{r1} + \frac{T_s}{2} + mT_s\right), & T_{r1} \le t'_K < T_s \end{cases} \quad (10)$$

$$i_2(t) = \begin{cases} \frac{\left(V_{\mathrm{OUT}}+V_{2,\mathrm{ini}}\right)}{2V_{\mathrm{OUT}}} i_{\mathrm{step}}\left(t-T_{r1}\right) - \sum_{m=1}^{K-1} i_{\mathrm{step}}\left(t'_K - T_{r1} + mT_s\right) \\ \qquad +\sum_{m=1}^{K-1} i_{\mathrm{step}}\left(t'_K - T_{r1} + \frac{T_s}{2} + mT_s\right), & 0 \le t'_K < T_{r1}-\frac{T_s}{2} \\ \frac{\left(V_{\mathrm{OUT}}+V_{2,\mathrm{ini}}\right)}{2V_{\mathrm{OUT}}} i_{\mathrm{step}}\left(t-T_{r1}\right) - \sum_{m=1}^{K-1} i_{\mathrm{step}}\left(t'_K - T_{r1} + mT_s\right) \\ \qquad +\sum_{m=0}^{K-1} i_{\mathrm{step}}\left(t'_K - T_{r1} + \frac{T_s}{2} + mT_s\right), & T_{r1}-\frac{T_s}{2} \le t'_K < T_{r1} \\ \frac{\left(V_{\mathrm{OUT}}+V_{2,\mathrm{ini}}\right)}{2V_{\mathrm{OUT}}} i_{\mathrm{step}}\left(t-T_{r1}\right) - \sum_{m=0}^{K-1} i_{\mathrm{step}}\left(t'_K - T_{r1} + mT_s\right) \\ \qquad +\sum_{m=0}^{K-1} i_{\mathrm{step}}\left(t'_K - T_{r1} + \frac{T_s}{2} + mT_s\right), & T_{r1} \le t'_K < T_s \end{cases}. \quad (11)$$

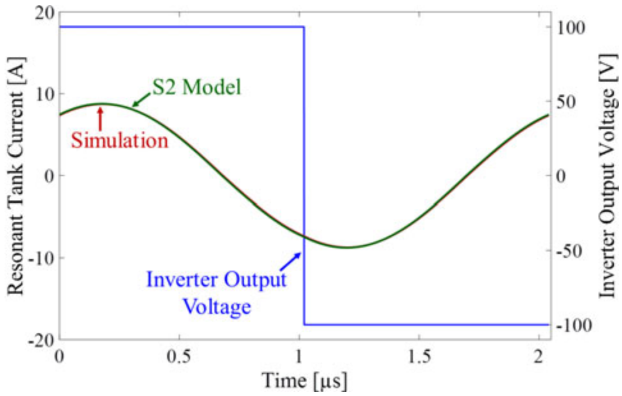

Fig. 8. Comparison of S2-modeled and LTSpice-simulated tank current waveforms of the SRC operating in steady state in a below-resonance mode ($k = 1$ CCM) with the same input and output voltages, tank component values, and switching frequency as in Fig. 7.

resonant tank current of the SRC are half-period symmetric. For the SRC operating in the above-resonance mode ($k = 0$ CCM), the integral in (14) can be evaluated using the expression for the tank current $i(t)$ obtained by adding (7) and (8), resulting in the following closed-form expression for output power in the $k = 0$ CCM mode:

$$P_{\mathrm{OUT},0} = \frac{4V_{\mathrm{IN}}V_{\mathrm{OUT}}}{\omega_d^2 L T_s}\left[\frac{\cos\left(\frac{\omega_d T_s}{4} - \omega_d T_{r0}\right)}{\cos\frac{\omega_d T_s}{4}} - 1\right]. \tag{15}$$

For the SRC operating in the below-resonance mode ($k = 1$ CCM), the integral in (14) can be evaluated using the expression for $i(t)$ obtained by adding (7) and (12), resulting in the following expression for output power in the $k = 1$ CCM mode:

$$P_{\mathrm{OUT},1} = \frac{4V_{\mathrm{IN}}V_{\mathrm{OUT}}}{\omega_d^2 L T_s}\left[1 - \frac{\cos\left(\omega_d T_{r1} - \frac{3\omega_d T_s}{4}\right)}{\cos\frac{\omega_d T_s}{4}}\right]. \tag{16}$$

Given the tank component values, dc input and output voltages, and the switching frequency of the SRC, the output power expressions in (15) and (16) can be used to directly identify the operating mode of the converter. First, the damped natural frequency of the resonant tank ω_d is computed using the inductance, capacitance, and resistance values of the tank, as defined in (4). The time lag of the rectifier input voltage in the two operating modes ($T_{r,0}$ in the $k = 0$ CCM mode and T_{r1} in the $k = 1$ CCM mode) is then computed using (9) and (13). Finally, the predicted output power of the SRC in the two modes is evaluated using (15) and (16). Depending on the switching frequency f_s (and hence the switching period $T_s = 1/f_s$), the predicted output power given by one of these equations comes out to be positive, while the other is negative. Since the SRC of Fig. 2 has a diode rectifier, its output power must be positive. Therefore, the equation ((15) or (16)) that predicts positive output power corresponds to the correct operating mode. As an example, the output power of the SRC of Fig. 2 is evaluated using both (15) and (16) for the same input and output voltage specifications and tank component values as those considered in the previous two sections, at two switching frequencies: 490 and 505 kHz. For the 490-kHz case, (15) predicts an output power of $P_{\mathrm{OUT},0} = -278.2$ W, while (16) predicts an output power of $P_{\mathrm{OUT},1} = 278.2$ W. Therefore, at this switching frequency, the SRC operates in the below-resonance $k = 1$ CCM mode, and the tank current expressions of (7) and (12) apply. When operating at 505 kHz, the output power predicted by (15) is $P_{\mathrm{OUT},0} = 560$ W, while that predicted by (16) is $P_{\mathrm{OUT},1} = -560$ W. Therefore, the SRC operates in the above-resonance $k = 0$ CCM mode at this switching frequency, and the tank current expressions of (7) and (8) can be utilized to predict its behavior.

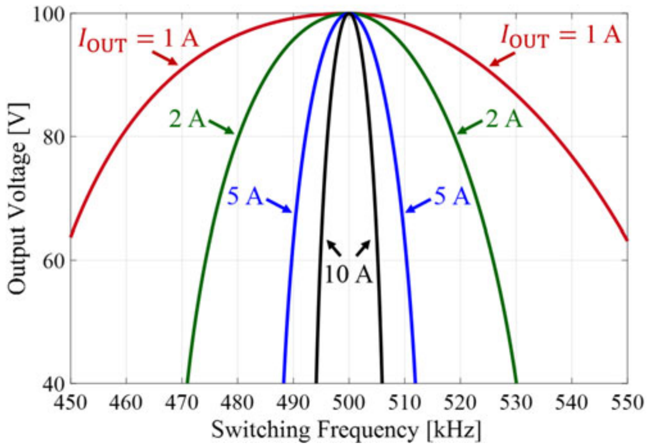

Fig. 9. S2-predicted output voltage of the SRC of Fig. 2 as a function of its switching frequency for various values of the output current I_{OUT}, when operating with an input voltage of V_{IN} of 100 V and tank component values of $L = 100\ \mu$H and $C = 1.0132$ nF (resulting in a resonant frequency of 500 kHz).

D. Determination of the Output Voltage of the SRC

The expressions for the output power of the SRC, given in (15) and (16), can also be utilized, in conjunction with the corresponding rectifier time lag expressions of (9) and (13), to express the output voltage of the SRC V_{OUT} in terms of its output current I_{OUT} ($= P_{\mathrm{OUT}}/V_{\mathrm{OUT}}$), input voltage V_{IN}, switching frequency f_s, and tank parameters (inductance value L and damped natural frequency ω_d), as

$$V_{\mathrm{OUT}} = \begin{cases} \sqrt{\dfrac{V_{\mathrm{IN}}^2 - \left(V_{\mathrm{IN}} + \frac{I_{\mathrm{OUT}}\omega_d^2 L}{4f_s}\right)^2 \cos^2\frac{\omega_d}{4f_s}}{\sin^2\frac{\omega_d}{4f_s}}} & \text{in } k = 0 \text{ CCM} \\ \sqrt{\dfrac{V_{\mathrm{IN}}^2 - \left(V_{\mathrm{IN}} - \frac{I_{\mathrm{OUT}}\omega_d^2 L}{4f_s}\right)^2 \cos^2\frac{\omega_d}{4f_s}}{\sin^2\frac{\omega_d}{4f_s}}} & \text{in } k = 1 \text{ CCM.} \end{cases} \tag{17}$$

The output voltage of the SRC of Fig. 2, as predicted by (17) for the same input voltage and tank design as described earlier, is shown as a function of switching frequency, for various values of output current, in Fig. 9. As can be seen, when the switching frequency equals the tank resonant frequency (500 kHz), the output voltage equals the input voltage (100 V) for all values of the output current. As the switching frequency is increased above, or decreased below, the resonant frequency, the output voltage decreases. The larger the output current, the sharper the decrease in the output voltage. This is because a larger output current corresponds to a higher loaded quality factor of the series-resonant tank, which makes the voltage gain provided by the tank, and, hence, the output voltage of the converter, more

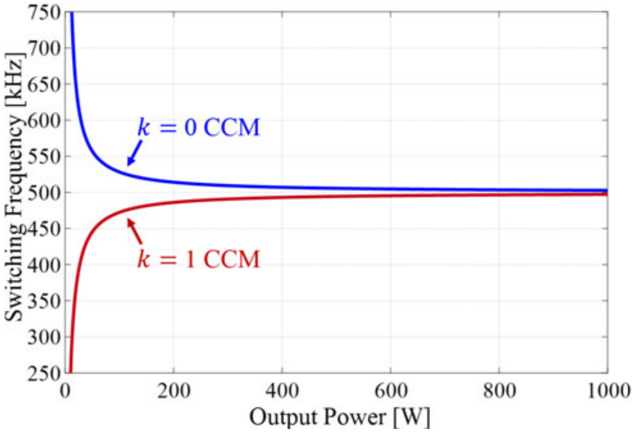

Fig. 10. S2-predicted switching frequency of the SRC of Fig. 2 as a function of output power. Here, the SRC is operating with an input voltage V_{IN} of 100 V and tank component values of $L = 100\ \mu$H and $C = 1.0132$ nF (resulting in a resonant frequency of 500 kHz).

sensitive to frequency variations. These trends in output voltage are similar to those predicted by simplified modeling approaches such as fundamental-frequency analysis; however, S2 analysis predicts the value of the output voltage much more accurately, particularly when the resonant tank of the SRC has a low quality factor and its currents are highly nonsinusoidal.

E. Determination of the Switching Frequency of the SRC

S2 analysis can also be utilized to determine the switching frequency f_s that the SRC needs to operate at to achieve a desired output power P_{OUT}. Due to the transcendental nature of the equations involved, it is difficult to obtain closed-form expressions for the switching frequency. However, the output power expressions in (15) and (16), together with the rectifier time lag expressions in (9) and (13), can be used to obtain the following implicit relationships:

$$\left(\frac{V_{\text{OUT}}}{V_{\text{IN}}}\right)^2 \sin^2\frac{\omega_d}{4f_s} + \left(1 + \frac{P_{\text{OUT}}\omega_d^2 L}{4V_{\text{IN}}V_{\text{OUT}}f_s}\right)^2 \cos^2\frac{\omega_d}{4f_s} = 1 \quad \text{in } k = 0 \text{ CCM}$$

$$\left(\frac{V_{\text{OUT}}}{V_{\text{IN}}}\right)^2 \sin^2\frac{\omega_d}{4f_s} + \left(1 - \frac{P_{\text{OUT}}\omega_d^2 L}{4V_{\text{IN}}V_{\text{OUT}}f_s}\right)^2 \cos^2\frac{\omega_d}{4f_s} = 1 \quad \text{in } k = 1 \text{ CCM.} \tag{18}$$

The above equations can be solved numerically to obtain the switching frequency required to attain a certain power level, as shown in Fig. 10 for the SRC of Fig. 2 operating with the input and output voltages and tank design described earlier, for both the above-resonance $k = 0$ CCM and below-resonance $k = 1$ CCM operating modes. As can be seen, for any desired output power level, the SRC can operate at two frequencies—a higher frequency in the $k = 0$ CCM mode, and a lower frequency in the $k = 1$ CCM mode. The choice between these two frequencies is governed by efficiency considerations. In the higher frequency $k = 0$ CCM mode, the inverter output current of the SRC lags the inverter output voltage (see Fig. 5). This enables the inverter transistors to operate with zero-voltage switching (ZVS), resulting in relatively low switching losses. However, the higher operating frequency can also lead to relatively large inductor losses. For the same inductor design, the inductor losses are smaller in the lower frequency $k = 1$ CCM mode; however, since the inverter output current leads the inverter output voltage in this mode (see Fig. 8), ZVS cannot be achieved and switching losses are higher. The S2-predicted inverter output current waveforms can be utilized, in conjunction with an accurate loss model, to inform the choice of the switching frequency in the presence of these tradeoffs.

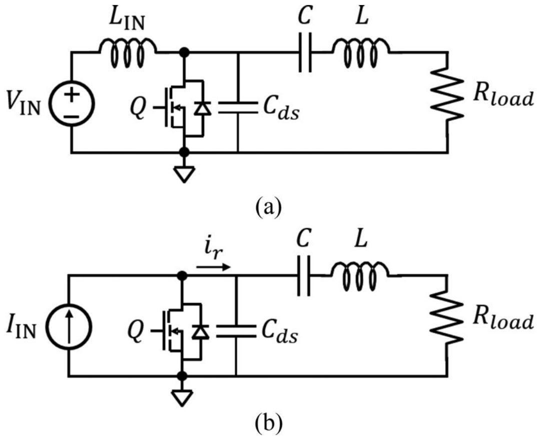

Fig. 11. Example class-E inverter with: (a) dc voltage source V_{IN} and large inductor L_{IN} at its input and (b) dc input current source I_{IN} modeling the dc input voltage source and inductor.

IV. APPLICABILITY OF S2 ANALYSIS

S2 analysis is applicable to all resonant converters that satisfy two requirements. First, it should be possible to model the resonant converter as a network which is LTI driven by a collection of independent voltage and/or current sources, so that superposition applies. Second, the voltage and/or current sources driving the network must be rectangular-wave sources so that they can be modeled as a series of time-shifted steps whose individual responses can be summed together. Resonant converters driven by class-D inverters and loaded by class-D rectifiers, including the SRC discussed above, satisfy these two requirements in most cases (with the one exception discussed later in this section), and can be modeled using S2 analysis. However, resonant converters containing inverters or rectifiers belonging to class-E, class-F, and other related types [40]–[44], typically do not satisfy one or both of the requirements of S2 analysis. For instance, consider the class-E inverter shown in Fig. 11(a). The input of this inverter comprises a voltage source followed by a large inductor, and can be modeled as a current source, as shown in Fig. 11(b). The current that feeds the resonant network (shown as i_r in Fig. 11(b)) equals the dc input current I_{IN} when the transistor Q is off, and zero when the transistor is on. Therefore, the resonant network of the class-E inverter is fed by a rectangular-wave current source, satisfying one of the requirements of S2 analysis. However, the resonant network itself changes during the converter's operation, as shown in Fig. 12: the capacitor C_{ds} is a part of the

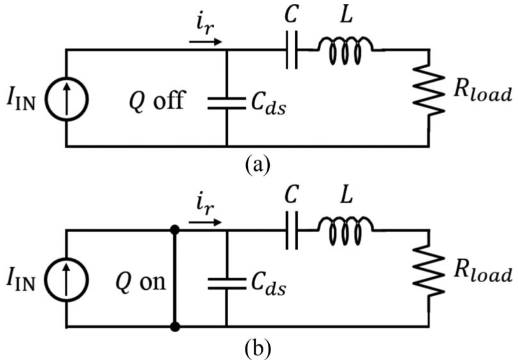

Fig. 12. Equivalent circuit of the class-E inverter of Fig. 7 with: (a) Transistor turned off and (b) Transistor turned on.

resonant network when the transistor is off, but is shorted out when the transistor is on. Therefore, the resonant network of the class-E inverter is not LTI, and S2 analysis is not applicable.

S2 analysis is also not applicable when the class-D inverter and/or rectifier of a resonant converter operates in a discontinuous-conduction mode (DCM). This is because the voltage/current at the output port of a class-D inverter (or at the input port of a class-D rectifier) operating in DCM is not well modeled by a rectangular-wave source. For example, consider an *LLC* resonant converter with a passive (diode) rectifier operating below resonance. In this operating mode, the rectifier of the *LLC* converter goes into DCM [10]. During the rectifier's nonconducting period, the voltage at its input port is not prespecified. Hence, the rectifier input voltage in an *LLC* converter operating below resonance cannot be modeled as a rectangular-wave source, which makes S2 analysis non-applicable. Furthermore, if the parasitic output capacitances of the rectifier diodes are also considered, then these capacitances become a part of the converter's resonant tank during the rectifier's nonconducting period; hence, the LTI requirement of S2 analysis is also violated.

The LTI requirement of S2 analysis also implies that the effect of dead times on the resonant network waveforms should be negligible. This is because during the dead time, the output capacitances of the inverter and rectifier transistors and diodes become a part of the resonant network. However, if the dead times in a resonant converter are short, they do not substantially impact the converter waveforms, and S2 analysis can be utilized. Furthermore, short dead times allow the voltage and/or current sources driving the resonant network to be accurately modeled as rectangular-wave sources, also fulfilling the second requirement of S2 analysis. This is discussed in more detail in the next section.

Therefore, in summary, S2 analysis can be utilized to analyze resonant converters with LTI networks, and class-D inverters and rectifiers operating in CCM with short dead times. Note that the class-D inverters can be either voltage or current driven, and the class-D rectifiers can be either voltage or current loaded. Under these conditions, S2 analysis can provide closed-form expressions for resonant network waveforms even for converters containing high-order resonant networks and multiple inverters and/or rectifiers, as described in the next section.

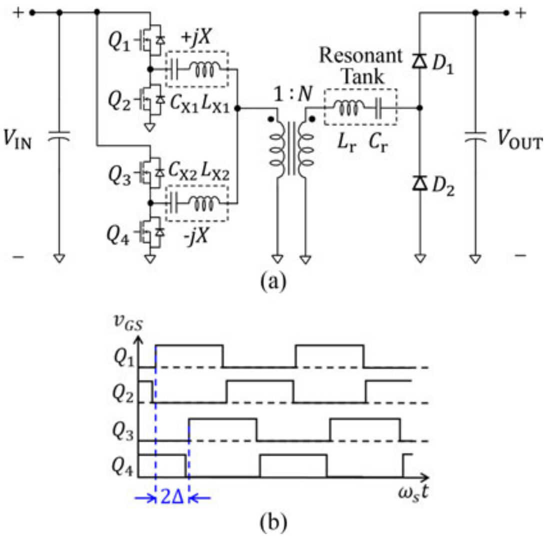

Fig. 13. One example ICN resonant converter [31], appropriate for voltage step up: (a) Converter topology and (b) switch gating signals.

V. Application to ICN Resonant Converter

As stated above, S2 analysis can be readily applied to high-order resonant converters with advanced topologies. In this section, this approach is applied to a recently proposed multi-inverter multi-element resonant converter—the ICN resonant converter [31]–[38]. The ICN converter is capable of maintaining ZVS and near-zero-current switching (near-ZCS) across wide operating ranges. The ICN converter introduced in [31] is shown in Fig. 13. This converter is operated at a fixed switching frequency and each inverter is operated at a fixed duty ratio (∼50%). A combination of phase-shift control (for inverters) and burst-mode control (in which the converter is modulated on and off at a frequency much lower than its switching frequency) is used to regulate the output voltage and power of the ICN converter.

The equivalent model for the ICN converter of Fig. 13 is shown in Fig. 14, where the three voltage sources imposed on the resonant network are modeled by square-wave voltage sources: the output voltages of the top and bottom inverters are modeled by the sources v_1 and v_2, respectively, and the input voltage of the rectifier is modeled by the source v_3. As can be seen from Fig. 14(b), the output voltages of the two inverters are phase shifted with respect to one another by 2Δ (and hence time shifted by $\frac{2\Delta}{2\pi}T_s$, where T_s is the converter's switching period), and the rectifier input voltage lags the top inverter output voltage by time T_r. Given these time shifts, the three square-wave voltage sources of the ICN converter can be modeled by series of positive and negative steps, as given by (19)–(21) at the bottom of the next page. Here, $V_{1,\text{ini}}$ and $V_{2,\text{ini}}$ are the voltages at the outputs of the two inverters, and $V_{3,\text{ini}}$ is the voltage at the input of the rectifier before the converter is turned on, t is taken to be zero when the converter is turned on, $K(= 1, 2, 3, \ldots)$ is the number of the switching cycles that have passed since the converter was turned on, including the current switching cycle (the Kth switching cycle), and t'_K is the time elapsed within the current switch-

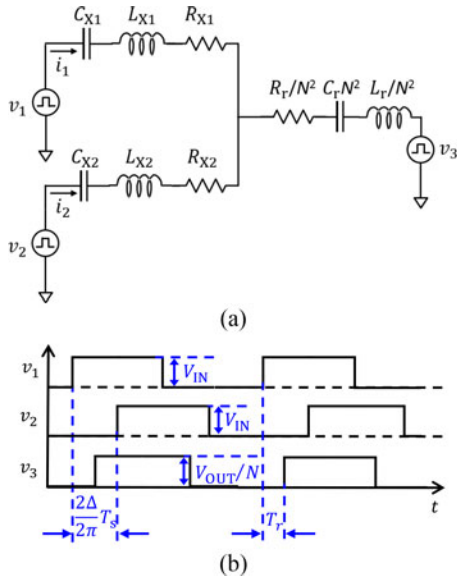

Fig. 14. Equivalent circuit model for the ICN converter of Fig. 9. (a) Resistors model converter losses. (b) Waveforms of voltage sources.

ing cycle. The relationship between t, t'_K, and K is the same as described for the SRC in the previous section, and given in (3).

Assuming that the resonant tanks of the ICN converter are lightly damped, each of the steps in the inverter and rectifier imposed voltages in (19)–(21) shown at the bottom of this page, produces a response in the inverter output currents of the ICN converter of the following form:

$$i_{xy,\text{step}}(t) = I_{xy1}e^{-\alpha_1 t}\sin\omega_1 t + I_{xy2}e^{-\alpha_2 t}\sin\omega_2 t. \tag{22}$$

Here, $i_{xy,\text{step}}(t)$ is the response of the inverter output current i_x to a step in the inverter/rectifier imposed voltage v_y. The magnitude of the voltage step equals the converter's input voltage V_{IN} when the step is in one of the inverter output voltages (see (19) and (20)), and the converter's output voltage V_{OUT} when the step is in the rectifier input voltage (see (21)). For instance, $i_{11,\text{step}}(t)$ is the response of the top inverter output current to a step in the top inverter output voltage, of the form $V_{\text{IN}}u(t)$. The parameters I_{xy1}, I_{xy2}, α_1, α_2, ω_1, and ω_2 in (22) depend on the ICN converter's input voltage, output voltage, reactive component values, transformer turns ratio, and converter losses. Expressions for these parameters, along with their derivations, are provided in Appendix B.

The inverter output currents of the ICN converter (i_1 and i_2 in Fig. 14) are obtained by summing all the step responses given by (22). This is done systematically by splitting the inverter output currents into three components, two generated as a response to the steps imposed by the two inverters (given in (19) and (20)), and the third generated by the steps imposed by the rectifier (given in (21)), as under

$$i_1(t) = i_{11}(t) + i_{12}(t) + i_{13}(t) \tag{23}$$

$$i_2(t) = i_{21}(t) + i_{22}(t) + i_{23}(t) \tag{24}$$

Here, $i_{xy}(t)$ is the component of i_x generated by v_y (where x signifies the two inverters and equals 1 or 2, and y signifies the two inverters and the rectifier and equals 1, 2 or 3, as shown in Fig. 14). The three components of the inverter output currents are individually expressed by (25)–(27) shown at the bottom of the next page. The expressions for the three components of the top and bottom inverter output currents of the ICN converter given in (25)–(27) can be simplified using the approach presented in

$$v_1(t) = \begin{cases} V_{1,\text{ini}} - V_{1,\text{ini}}u(t) + \sum_{m=0}^{N-1} V_{\text{IN}}u\left(t'_K + mT_s\right) \\ \quad - \sum_{m=1}^{N-1} V_{\text{IN}}u\left(t'_K - \frac{T_s}{2} + mT_s\right), & 0 \le t'_K < \frac{T_s}{2} \\ V_{1,\text{ini}} - V_{1,\text{ini}}u(t) + \sum_{m=0}^{N-1} V_{\text{IN}}u\left(t'_K + mT_s\right) \\ \quad - \sum_{m=0}^{N-1} V_{\text{IN}}u\left(t'_K - \frac{T_s}{2} + mT_s\right), & \frac{T_s}{2} \le t'_K < T_s \end{cases} \tag{19}$$

$$v_2(t) = \begin{cases} V_{2,\text{ini}} - V_{2,\text{ini}}u(t-2\Delta_t) + \sum_{m=1}^{N-1} V_{\text{IN}}u\left(t'_K - 2\Delta_t + mT_s\right) \\ \quad - \sum_{m=1}^{N-1} V_{\text{IN}}u\left(t'_K - 2\Delta_t - \frac{T_s}{2} + mT_s\right), & 0 \le t'_K < 2\Delta_t \\ V_{2,\text{ini}} - V_{2,\text{ini}}u(t-2\Delta_t) + \sum_{m=0}^{N-1} V_{\text{IN}}u\left(t'_K - 2\Delta_t + mT_s\right) \\ \quad - \sum_{m=1}^{N-1} V_{\text{IN}}u\left(t'_K - 2\Delta_t - \frac{T_s}{2} + mT_s\right), & 2\Delta_t \le t'_K < 2\Delta_t + \frac{T_s}{2} \\ V_{2,\text{ini}} - V_{2,\text{ini}}u(t-2\Delta_t) + \sum_{m=0}^{N-1} V_{\text{IN}}u\left(t'_K - 2\Delta_t + mT_s\right) \\ \quad - \sum_{m=0}^{N-1} V_{\text{IN}}u\left(t'_K - 2\Delta_t - \frac{T_s}{2} + mT_s\right), & 2\Delta_t + \frac{T_s}{2} \le t'_K < T_s \end{cases}, \tag{20}$$

$$v_3(t) = \frac{1}{N} \cdot \begin{cases} V_{3,\text{ini}} - V_{3,\text{ini}}u(t-T_r) + \sum_{m=1}^{N-1} V_{\text{OUT}}u\left(t'_K - T_r + mT_s\right) \\ \quad - \sum_{m=1}^{N-1} V_{\text{OUT}}u\left(t'_K - T_r - \frac{T_s}{2} + mT_s\right), & 0 \le t'_K < T_r \\ V_{3,\text{ini}} - V_{3,\text{ini}}u(t-T_r) + \sum_{m=0}^{N-1} V_{\text{OUT}}u\left(t'_K - T_r + mT_s\right) \\ \quad - \sum_{m=1}^{N-1} V_{\text{OUT}}u\left(t'_K - T_r - \frac{T_s}{2} + mT_s\right), & T_r \le t'_K < T_r + \frac{T_s}{2} \\ V_{3,\text{ini}} - V_{3,\text{ini}}u(t-T_r) + \sum_{m=0}^{N-1} V_{\text{OUT}}u\left(t'_K - T_r + mT_s\right) \\ \quad - \sum_{m=0}^{N-1} V_{\text{OUT}}u\left(t'_K - T_r - \frac{T_s}{2} + mT_s\right), & T_r + \frac{T_s}{2} \le t'_K < T_s \end{cases}. \tag{21}$$

Appendix A to yield closed-form expressions that describe the inverter output currents both during steady-state operation and during the startup transients of the burst-mode operation. For ease of analysis, these closed-form expressions can be split into their steady-state and transient components, shown as

$$i_{xy}(t) = i_{xys}(t) + i_{xyt}(t). \tag{28}$$

Here, $i_{xys}(t)$ and $i_{xyt}(t)$ represent the steady-state and transient components of $i_{xy}(t)$, respectively. As an example, the component of the top inverter current i_1 generated by the top inverter output voltage v_1, denoted by i_{11}, can be expressed in a closed form as the sum of its steady-state component i_{11s} and transient component i_{11t}, which are given by

$$i_{11s}(t) = \begin{cases} \dfrac{I_{111}\sin\left(\omega_1 t'_K - \frac{\omega_1 T_s}{4}\right)}{2\cos\left(\frac{\omega_1 T_s}{4}\right)} + \dfrac{I_{112}\sin\left(\omega_2 t'_K - \frac{\omega_2 T_s}{4}\right)}{2\cos\left(\frac{\omega_2 T_s}{4}\right)}, & 0 \le t'_K < \frac{T_s}{2} \\ \dfrac{I_{111}\sin\left(\frac{3\omega_1 T_s}{4} - \omega_1 t'_K\right)}{2\cos\left(\frac{\omega_1 T_s}{4}\right)} + \dfrac{I_{112}\sin\left(\frac{3\omega_2 T_s}{4} - \omega_2 t'_K\right)}{2\cos\left(\frac{\omega_2 T_s}{4}\right)}, & \frac{T_s}{2} \le t'_K < T_s \end{cases} \tag{29}$$

$$\begin{aligned} i_{11t}(t) = {} & \frac{V_{1,\text{ini}}}{V_{\text{IN}}} I_{111} e^{-\alpha_1 t} \sin\omega_1 t + \frac{V_{1,\text{ini}}}{V_{\text{IN}}} I_{112} e^{-\alpha_2 t} \sin\omega_2 t \\ & - \frac{I_{111}}{2\cos\left(\frac{\omega_1 T_s}{4}\right)} e^{-(K-1)\alpha_1 T_s} \sin\left(-\omega_1 t'_K - K\omega_1 T_s + \frac{3\omega_1 T_s}{4}\right) \\ & - \frac{I_{112}}{2\cos\left(\frac{\omega_2 T_s}{4}\right)} e^{-(K-1)\alpha_2 T_s} \sin\left(-\omega_2 t'_K - K\omega_2 T_s + \frac{3\omega_2 T_s}{4}\right). \end{aligned} \tag{30}$$

The first two terms on the right-hand side of (28) are the startup transients generated in the top inverter current i_1 by the initial value $V_{1,\text{ini}}$ of the top inverter output voltage v_1, and the remaining two terms describe the transients generated by the continuously imposed steps in v_1. It can be seen that all the terms in (30) contain decaying exponentials; therefore, the startup transients given in (30) die out in steady state, leaving behind the steady-state component given in (29). Closed-form expressions similar to (29) and (30) for all the components of the two inverter output currents of the ICN converter are derived in Appendix B.

It can be seen from Fig. 13 that the input current of the rectifier of the ICN converter is given by the sum of the two inverter output currents i_1 and i_2, scaled by the transformer's turns ratio N. Since the rectifier switches commutate when the rectifier input current is zero, the time lag T_r of the rectifier's input voltage can be found by solving the closed-form expressions for i_1 and i_2 for the condition that their scaled sum, $(i_1 + i_2)/N$, equals zero at the instant $t'_K = T_r$.

The closed-form expressions for the inverter output currents i_1 and i_2 of the ICN converter obtained using S2 analysis have several useful applications. For instance, these expressions can be utilized to optimize the ICN converter's design over a wide range of operating conditions. To demonstrate this, a 200-W 500-kHz ICN converter is designed to operate over an input voltage range of 25–40 V and output voltage range of 250–400 V. The first step in designing this converter is to select the transformer turns ratio N and the ICN differential reactance X (see Fig. 13). These are selected to ensure that the converter can deliver the required rated power (200 W), and that the delivered power has a flat profile, over the converter's entire operating range [31]. Given values for N and X (= 5.3 and 2 Ω for the

$$i_{x1}(t) = \begin{cases} -\frac{V_{1,\text{ini}}}{V_{\text{IN}}} i_{x1,\text{step}}(t) + \sum_{m=0}^{N-1} i_{x1,\text{step}}\left(t'_K + mT_s\right) \\ \quad -\sum_{m=1}^{N-1} i_{x1,\text{step}}\left(t'_K - \frac{T_s}{2} + mT_s\right), & 0 \le t'_K < \frac{T_s}{2} \\ -\frac{V_{1,\text{ini}}}{V_{\text{IN}}} i_{x1,\text{step}}(t) + \sum_{m=0}^{N-1} i_{x1,\text{step}}\left(t'_K + mT_s\right) \\ \quad -\sum_{m=0}^{N-1} i_{x1,\text{step}}\left(t'_K - \frac{T_s}{2} + mT_s\right), & \frac{T_s}{2} \le t'_K < T_s \end{cases} \tag{25}$$

$$i_{x2}(t) = \begin{cases} -\frac{V_{2,\text{ini}}}{V_{\text{IN}}} i_{x2,\text{step}}(t - 2\Delta_t) + \sum_{m=1}^{N-1} i_{x2,\text{step}}\left(t'_K - 2\Delta_t + mT_s\right) \\ \quad -\sum_{m=1}^{N-1} i_{x2,\text{step}}\left(t'_K - 2\Delta_t - \frac{T_s}{2} + mT_s\right), & 0 \le t'_K < 2\Delta_t \\ -\frac{V_{2,\text{ini}}}{V_{IN}} i_{x2,\text{step}}(t - 2\Delta_t) + \sum_{m=0}^{N-1} i_{x2,\text{step}}\left(t'_K - 2\Delta_t + mT_s\right) \\ \quad -\sum_{m=1}^{N-1} i_{x2,\text{step}}\left(t'_K - 2\Delta_t - \frac{T_s}{2} + mT_s\right), & 2\Delta_t \le t'_K < 2\Delta_t + \frac{T_s}{2} \\ -\frac{V_{2,\text{ini}}}{V_{\text{IN}}} i_{x2,\text{step}}(t - 2\Delta_t) + \sum_{m=0}^{N-1} i_{x2,\text{step}}\left(t'_K - 2\Delta_t + mT_s\right) \\ \quad -\sum_{m=0}^{N-1} i_{x2,\text{step}}\left(t'_K - 2\Delta_t - \frac{T_s}{2} + mT_s\right), & 2\Delta_t + \frac{T_s}{2} \le t'_K < T_s \end{cases} \tag{26}$$

$$i_{x3}(t) = \begin{cases} -\frac{V_{3,\text{ini}}}{V_{\text{OUT}}} i_{x3,\text{step}}(t - T_r) + \sum_{m=1}^{N-1} i_{x3,\text{step}}\left(t'_K - T_r + mT_s\right) \\ \quad \sum_{m=1}^{N-1} i_{x3,\text{step}}\left(t'_K - T_r - \frac{T_s}{2} + mT_s\right), & 0 \le t'_K < T_r \\ -\frac{V_{3,\text{ini}}}{V_{\text{OUT}}} i_{x3,\text{step}}(t - T_r) + \sum_{m=0}^{N-1} i_{x3,\text{step}}\left(t'_K - T_r + mT_s\right) \\ \quad -\sum_{m=1}^{N-1} i_{x3,\text{step}}\left(t'_K - T_r - \frac{T_s}{2} + mT_s\right), & T_r \le t'_K < T_r + \frac{T_s}{2} \\ -\frac{V_{3,\text{ini}}}{V_{\text{OUT}}} i_{x3,\text{step}}(t - T_r) + \sum_{m=0}^{N-1} i_{x3,\text{step}}\left(t'_K - T_r + mT_s\right) \\ \quad -\sum_{m=0}^{N-1} i_{x3,\text{step}}\left(t'_K - T_r - \frac{T_s}{2} + mT_s\right), & T_r + \frac{T_s}{2} \le t'_K < T_s \end{cases}. \tag{27}$$

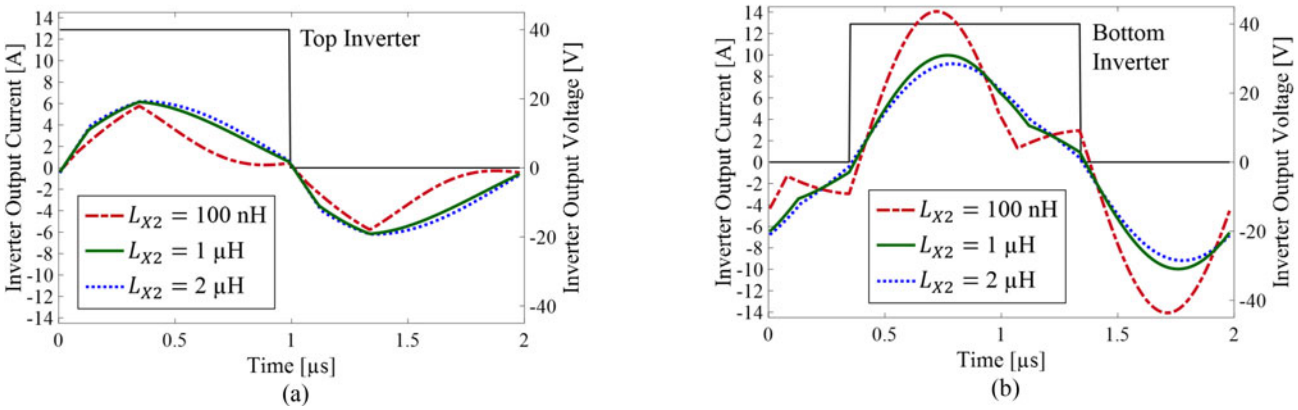

Fig. 15. S2-modeled inverter output current waveforms of the ICN converter operating in steady state with 40-V input voltage and 250-V output voltage for three different values of the inductance L_{X2}: (a) Top inverter and (b) bottom inverter.

above specifications, respectively), the next step is to select the inductance and capacitance values for the three resonant tanks of the ICN converter. These inductance and capacitance values must satisfy the following relationships:

$$\omega_s L_{X1} - \frac{1}{\omega_s C_{X1}} = X \tag{31}$$

$$\omega_s L_{X2} - \frac{1}{\omega_s C_{X2}} = -X \tag{32}$$

$$\omega_s L_r = \frac{1}{\omega_s C_r}. \tag{33}$$

Here, ω_s is the angular switching frequency of the converter. Each of the above design relationships can be satisfied by various combinations of inductance and capacitance values. To select the combinations that result in the highest converter efficiency, an iterative procedure based on S2 analysis is employed, as described below.

The three inductance values (L_{X1}, L_{X2}, and L_r) are swept over wide ranges, with the corresponding capacitance values (C_{X1}, C_{X2}, and C_r) selected to satisfy (31)–(33). For each inductance–capacitance combination, waveforms for the output currents of the two inverters i_1 and i_2 are obtained using the S2-modeled closed-form expressions. As an example, consider Fig. 15, which shows the S2-modeled inverter output current waveforms at a particular operating point ($V_{\mathrm{IN}} =$ 40 V, $V_{\mathrm{OUT}} = 250$ V) for three different values of the inductance L_{X2}, with the corresponding value of the capacitance C_{X2} chosen to satisfy (32), and the other inductance and capacitance values held constant. It can be seen from Fig. 15(a) and (b) that for a very low value of L_{X2} (100 nH), the inverter output currents are highly nonsinusoidal and unbalanced—the bottom inverter (see Fig. 15(b)) has a much higher current than the top inverter (see Fig. 15(a)). This unbalanced distribution of currents, and hence, losses between the two inverters typically translates to a poor overall converter efficiency. As the value of L_{X2} is increased, the currents assume more sinusoidal shapes and become better balanced, with potential efficiency benefits. However, higher inductance values also typically translate to larger magnetic losses, offsetting this advantage. Furthermore, as can be seen from Fig. 15, the improvement in the current waveforms reaches a point of diminishing returns beyond a value of L_{X2} around 1 μH. This analysis is quantified using an accurate loss model [31] and repeated over the entire operating range of the ICN converter. The resultant value of L_{X2} that yields the highest efficiency over the converter's operating range comes out to be 0.84 μH, and the capacitance C_{X2} is selected to be 68 nF in accordance with (32). The optimal inductance and capacitance values of the other two resonant tanks are similarly selected as $L_{X1} = 1.38$ μH, $C_{X1} = 141$ nF, $L_r = 20.8$ μH, and $C_r = 4.9$ nF. The closed-form expressions provided by S2 analysis allow this comprehensive design optimization to be performed in an automated fashion with very low computation time and minimal effort on the part of the circuit designer.

An ICN converter having the above optimized design is simulated in LTSpice, and the simulated waveforms of the top and bottom inverter currents are compared to those predicted by S2 analysis, as shown for two corner operating points of the converter—40-V input and 250-V output, and 25-V input and 400-V output—in Fig. 16. As can be seen, the S2-modeled waveforms very closely match the LTSpice-simulated waveforms.

To further validate the accuracy and demonstrate the utility of S2 analysis, a prototype ICN converter is designed, built, and tested. The inductance and capacitance values of the prototype converter are close to the aforementioned optimized values, with one difference being that the capacitor C_r is selected to have a slightly smaller value of 4.66 nF to resonate out the leakage inductance of the prototype transformer. The prototype converter is designed for a switching frequency of 500 kHz, and it is operated at a slightly higher frequency of 505 kHz in order to achieve ZVS of the inverter transistors. This switching frequency corresponds to a switching period of 1980 ns; in comparison, the dead times employed in the prototype ICN converter are of the order of only 50 ns (approximately 2.5% of the switching period), as shown in Fig. 17. These relatively short dead times have a negligible impact on the ICN converter's waveforms, and allow the inverter output voltages of the converter to be accurately modeled as rectangular-wave sources (see Fig. 17), as required by S2 analysis. The S2-modeled steady-state waveforms of the

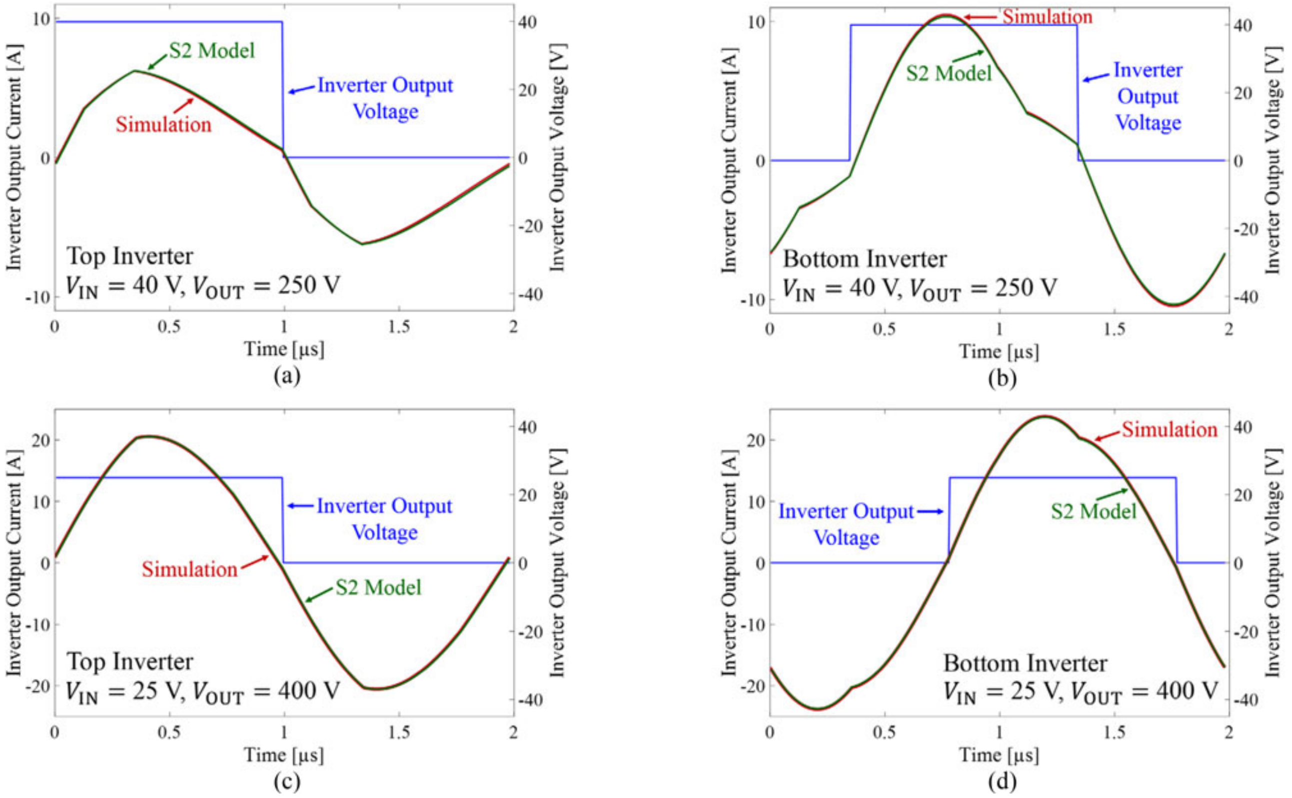

Fig. 16. Comparison of S2-modeled and LTSpice-simulated inverter output current waveforms of the ICN resonant converter of Fig. 9 operating in steady state with: (a) and (b) 40-V input voltage and 250-V output voltage, and (c) and (d) 25-V input voltage and 400-V output voltage. The converter's switching frequency is 505 kHz.

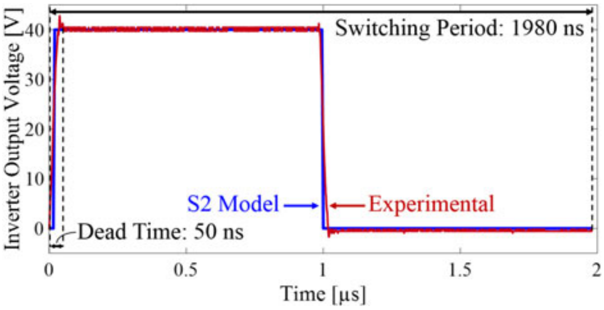

Fig. 17. Comparison of modeled and experimental output voltage of the top inverter of the ICN converter operating at 40-V input voltage and 250-V output voltage, demonstrating that owing to the relatively short dead time, the inverter output voltage can be accurately modeled as a rectangular-wave voltage source.

top and bottom inverter currents of the ICN converter are compared with the measured waveforms of the prototype converter operating at 40-V input voltage and 250-V output voltage, and at 25-V input voltage and 400-V output voltage in Fig. 18. As can be seen in Fig. 18, while the shapes of the S2-modeled waveforms are similar to those of the experimental waveforms, there is a significant difference in magnitude between the two. Closer examination revealed that this difference is due to the parasitic capacitances of the rectifier diodes used in the prototype converter. The charging and discharging of these parasitic capacitances during the rectifier commutations introduces extra delay into the rectifier switching time T_r. The delay ΔT_r can be approximated by the time required to discharge the parasitic capacitances of the rectifier diodes to half of the output voltage, and can be obtained from

$$\int_{T_r}^{T_r+\Delta T_r} \frac{i_1+i_2}{N}dt = 2C_{\text{diode}}V_{\text{OUT}} \times \frac{1}{2} \tag{34}$$

where C_{diode} is the parasitic capacitance of the rectifier diode. This equation neglects the slight change in the rectifier input current during the delay (ΔT_r) and calculates the charge needed to bring the rectifier input voltage to half the output voltage. The actual time lag of the rectifier input voltage with respect to the top inverter output voltage is given by $T_r + \Delta T_r$. After incorporating this new time lag into the S2 analysis of the ICN converter, the modeled waveforms of the converter are again compared to their experimental counterparts, as shown in Fig. 19. As can be seen, the modeled waveforms now match the experimental waveforms highly accurately.

The experimental and modeled burst-mode startup waveforms of the ICN converter are also compared, as shown for the ICN converter operating at two of its corner operating points—25-V input and 400-V output, and 40-V input and 400-V output—in Fig. 20. Again, it is apparent that excellent agreement exists between the modeled and experimental waveforms. This ability of S2 analysis to accurately predict converter waveforms makes it highly suitable for optimizing the design of resonant converters.

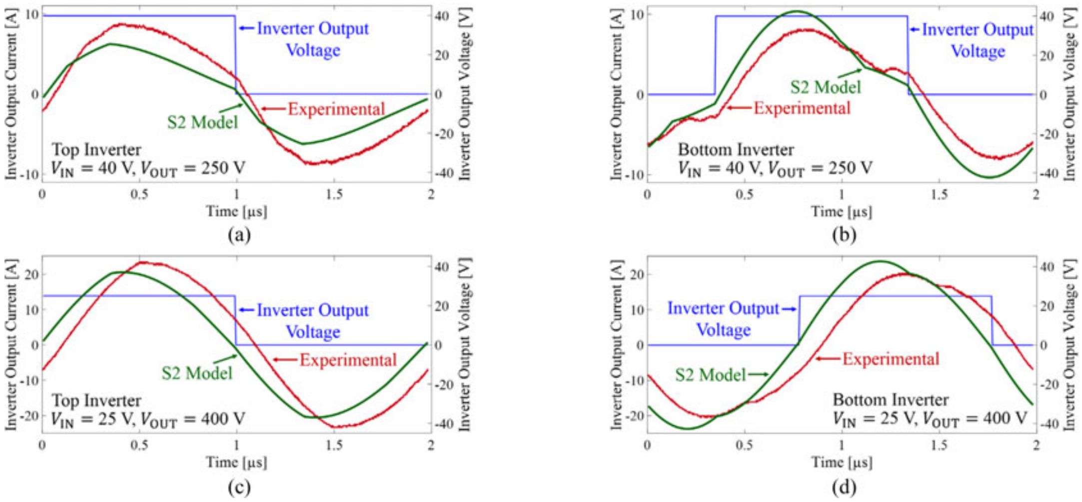

Fig. 18. Comparison of modeled and experimental steady-state waveforms of the ICN converter operating at: (a) and (b) 40-V input and 250-V output, and (c) and (d) 25-V input and 400-V output. Here, the S2 model assumes that the rectifier of the ICN converter has ideal diodes.

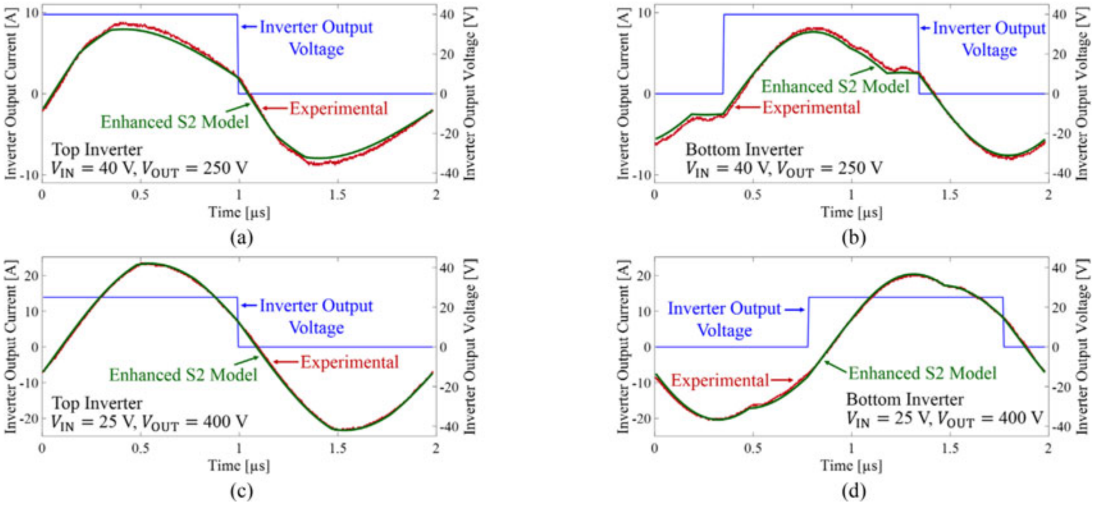

Fig. 19. Comparison of modeled and experimental steady-state waveforms of the ICN converter operating at: (a) and (b) 40-V input and 250-V output, and (c) and (d) 25-V input and 400-V output. Here, the S2 model incorporates the effective delay in rectifier switching caused by the charging and discharging of the parasitic capacitances of the rectifier diodes.

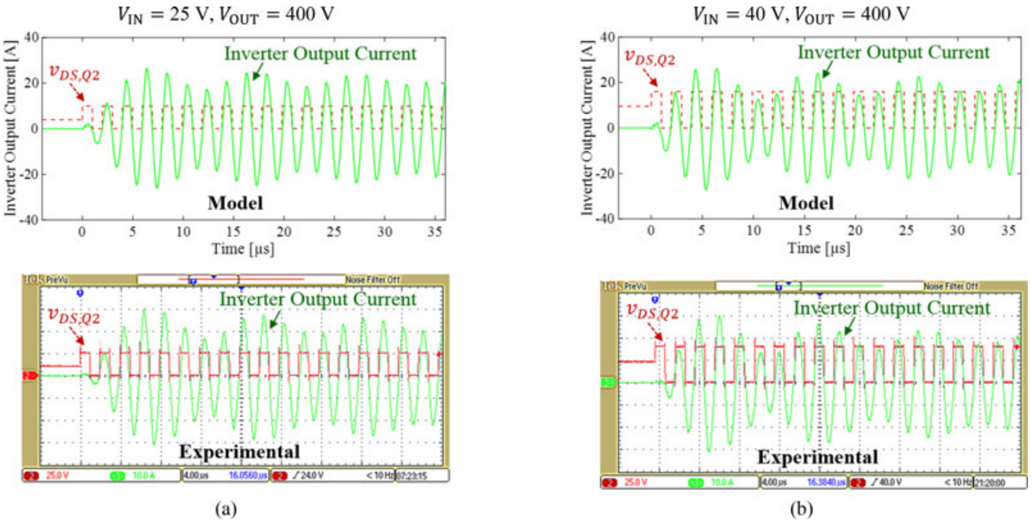

Fig. 20. Comparison of modeled and experimental burst-mode startup waveforms of the top inverter of the ICN converter operating at: (a) 25-V input and 400-V output, and (b) 40-V input and 400-V output.

VI. CONCLUSION

This paper introduces a new analysis approach to modeling resonant converters that can be used to determine closed-form expressions for the exact resonant network waveforms. This approach, based on the superposition of step responses to inverter and rectifier imposed steps, can easily be applied to resonant converters with high-order resonant networks, multiple inverters, and/or rectifiers. The proposed analysis approach is applied to an SRC, wherein it is used to determine accurate closed-form expressions for its tank current in different operating modes. These expressions are utilized to draw insights that help identify the converter's operating mode, and determine associated expressions for its output voltage and the switching frequency required to achieve a desired output power. The proposed approach is also applied to the multi-inverter multi-element ICN resonant converter, wherein it is used to derive closed-form expressions for the converter's currents. These expressions are utilized to evaluate the behavior and optimize the design of an ICN resonant converter. A prototype 200-W 500-kHz ICN resonant converter optimized using the proposed approach is used to validate the modeling results. It is shown that there is excellent agreement between the experimental and modeled waveforms during steady-state operation and during startup.

APPENDIX A
CLOSED-FORM EXPRESSION FOR THE SUMMATION OF TIME-SHIFTED DECAYING SINUSOIDS

This appendix presents a procedure to simplify the summation of a series of decaying sinusoidal functions into a closed-form expression. Consider a summation of a series of time-shifted decaying sinusoidal functions, given as

$$y_{\text{sum}}(t) = \sum_{m=0}^{K-1} e^{-\alpha\left(t'_K + mT_s\right)} \sin \omega_d \left(t'_K + mT_s\right). \tag{35}$$

Using Euler's formula ($e^{j\theta} = \cos\theta + j\sin\theta$), (35) can be expressed as

$$y_{\text{sum}}(t) = \sum_{m=0}^{K-1} e^{-\alpha\left(t'_K + mT_s\right)} \frac{e^{j\omega_d\left(t'_K + mT_s\right)} - e^{-j\omega_d\left(t'_K + mT_s\right)}}{2j}. \tag{36}$$

Rearranging (36) yields

$$\begin{aligned} y_{\text{sum}}(t) = {} & \frac{e^{(-\alpha + j\omega_d)t'_K}}{2j} \sum_{m=0}^{K-1} e^{(-\alpha + j\omega_d)mT_s} \\ & - \frac{e^{(-\alpha - j\omega_d)t'_K}}{2j} \sum_{m=0}^{K-1} e^{(-\alpha - j\omega_d)mT_s}. \end{aligned} \tag{37}$$

Under the light damping condition ($\alpha \ll \omega_{\text{d}}$), (37) can be simplified to

$$\begin{aligned} y_{\text{sum}}(t) = {} & \frac{e^{j\omega_d t'_K}}{2j} \frac{1 - e^{-\alpha(K-1)T_s} \cdot e^{j\omega_d(K-1)T_s}}{1 - e^{j\omega_d T_s}} \\ & - \frac{e^{-j\omega_d t'_K}}{2j} \frac{1 - e^{-\alpha(K-1)T_s} \cdot e^{-j\omega_d(K-1)T_s}}{1 - e^{-j\omega_d T_s}} \end{aligned} \tag{38}$$

which can be alternatively expressed as (39) shown at the bottom of this page.

Letting $A = [e^{j\omega_d t'_K}][1 - e^{-\alpha(K-1)T_s} \cdot e^{j\omega_d(K-1)T_s}][1 - e^{-j\omega_d T_s}]$, (39) can be more concisely written as

$$y_{\text{sum}}(t) = \frac{1}{2j} \frac{A - A^*}{\left[1 - e^{j\omega_d T_s}\right]\left[1 - e^{-j\omega_d T_s}\right]}. \tag{40}$$

Using the double angle trigonometric identity $\cos 2\theta = 1 - 2\sin^2\theta$, (40) can be further simplified into

$$y_{\text{sum}}(t) = \frac{1}{8j} \cdot \frac{A - A^*}{\sin^2\left(\frac{\omega_d T_s}{2}\right)}. \tag{41}$$

By expanding A and using Euler's formula, $A - A^*$ can be expressed as

$$\begin{aligned} A - A^* = 4j \Bigg[& \cos\left(\omega_d t'_K - \frac{\omega_d T_s}{2}\right) \sin\left(\frac{\omega_d T_s}{2}\right) - e^{-\alpha(K-1)T_s} \\ & \times \cos\left(\omega_d t'_K - \omega_d T_s + \omega_d K T_s - \frac{\omega_d T_s}{2}\right) \sin\left(\frac{\omega_d T_s}{2}\right)\Bigg]. \end{aligned} \tag{42}$$

Substituting (42) into (41) yields (43), shown at the bottom of this page.

When K approaches infinity, that is, as the converter reaches steady state, (43) can be further simplified into

$$y_{\text{sum}}(t) = \frac{\cos\left(\omega_d t'_K - \frac{\omega_d T_s}{2}\right)}{2\sin\left(\frac{\omega_d T_s}{2}\right)}. \tag{44}$$

$$\begin{aligned} & y_{\text{sum}}(t) \\ & = \frac{1}{2j} \frac{\left[e^{j\omega_d t'_K}\right]\left[1 - e^{-\alpha(K-1)T_s} \cdot e^{j\omega_d(K-1)T_s}\right]\left[1 - e^{-j\omega_d T_s}\right] - \left[e^{-j\omega_d t'_K}\right]\left[1 - e^{-\alpha(K-1)T_s} \cdot e^{-j\omega_d(K-1)T_s}\right]\left[1 - e^{j\omega_d T_s}\right]}{\left[1 - e^{j\omega_d T_s}\right]\left[1 - e^{-j\omega_d T_s}\right]}. \end{aligned} \tag{39}$$

$$y_{\text{sum}}(t) = \frac{\cos\left(\omega_d t'_K - \frac{\omega_d T_s}{2}\right) - e^{-\alpha(K-1)T_s} \cos\left(\omega_d t'_K + \omega_d K T_s - \omega_d T_s - \frac{\omega_d T_s}{2}\right)}{2\sin\left(\frac{\omega_d T_s}{2}\right)}. \tag{43}$$

APPENDIX B
DERIVATIONS OF EXPRESSIONS FOR INVERTER OUTPUT CURRENTS OF THE ICN CONVERTER

This appendix derives closed-form expressions for the two inverter output currents of the ICN converter i_1 and i_2, as shown in Fig. 14. The derivation begins by analyzing the ICN converter model of Fig. 14 in the frequency domain to obtain the various parameters in (22). The inverter output currents can be expressed in the frequency domain as

$$\begin{aligned} i_1(s) &= \frac{v_1(s)[Z_2(s)+Z_3(s)]}{Z(s)} - \frac{v_2(s)Z_3(s)}{Z(s)} \\ &\quad - \frac{v_3(s)Z_2(s)}{Z(s)} \qquad (45) \\ i_2(s) &= \frac{v_2(s)[Z_1(s)+Z_3(s)]}{Z(s)} - \frac{v_1(s)Z_3(s)}{Z(s)} \\ &\quad - \frac{v_3(s)Z_1(s)}{Z(s)}. \qquad (46) \end{aligned}$$

Here, $Z_1(s)$, $Z_2(s)$, and $Z_3(s)$ are the impedances of the three resonant tanks, given by

$$Z_1(s) = L_{X1}s + R_{X1} + \frac{1}{sC_{X1}} \qquad (47)$$

$$Z_2(s) = L_{X2}s + R_{X2} + \frac{1}{sC_{X2}} \qquad (48)$$

$$Z_3(s) = \frac{L_r}{N^2}s + \frac{R_r}{N^2} + \frac{1}{sC_rN^2} \qquad (49)$$

and $Z(s)$ is given by

$$Z(s) = Z_1(s)Z_2(s) + Z_1(s)Z_3(s) + Z_2(s)Z_3(s). \qquad (50)$$

Rearranging (45) and (46), the inverter output currents can be expressed as

$$\begin{aligned} i_1(s) &= \frac{s}{f(s)}([f_2(s)+f_3(s)]v_1(s) - f_3(s)v_2(s) \\ &\quad - f_2(s)v_3(s)) \qquad (51) \\ i_2(s) &= \frac{s}{f(s)}([f_1(s)+f_3(s)]v_2(s) - f_3(s)v_1(s) \\ &\quad - f_1(s)v_3(s)) \qquad (52) \end{aligned}$$

where $f_1(s)$, $f_2(s)$, and $f_3(s)$ are given by

$$f_1(s) = L_{X1}s^2 + R_{X1}s + \frac{1}{C_{X1}} \qquad (53)$$

$$f_2(s) = L_{X2}s^2 + R_{X2}s + \frac{1}{C_{X2}} \qquad (54)$$

$$f_3(s) = \frac{L_r}{N^2}s^2 + \frac{R_r}{N^2}s + \frac{1}{C_rN^2} \qquad (55)$$

and $f(s)$ is given by

$$f(s) = f_1(s)f_2(s) + f_1(s)f_3(s) + f_2(s)f_3(s). \qquad (56)$$

The parameters in (22) can now be systematically obtained by applying a step to one of the inverter/rectifier switch-node voltages, while the other two voltages are set to zero. For instance, consider a step of magnitude V_{IN} in the top inverter switch-node voltage, that is, $v_1(s) = \frac{V_{\mathrm{IN}}}{s}$, while $v_2(s) = 0$ and $v_3(s) = 0$. Applying these conditions to (51) and (52), the responses of the two inverter output currents to the step in $v_1(s)$ are given by

$$i_{11,\mathrm{step}}(s) = V_{\mathrm{IN}}\frac{f_2(s)+f_3(s)}{f(s)} \qquad (57)$$

$$i_{21,\mathrm{step}}(s) = V_{\mathrm{IN}}\frac{-f_3(s)}{f(s)}. \qquad (58)$$

It can be seen from (57) and (58) that the poles of $i_{11,\mathrm{step}}(s)$ and $i_{21,\mathrm{step}}(s)$ are given by the two pairs of complex-conjugate roots of the fourth-order polynomial $f(s)$. The absolute value of the real parts of these poles correspond to the exponential coefficients (α_1 and α_2), while the absolute value of the imaginary parts correspond to the damped frequencies (ω_1 and ω_2) in (22). Values for the parameters α_1, α_2, ω_1, and ω_2 can be obtained by numerically solving $f(s) = 0$. This procedure is repeated by applying steps to the bottom inverter and rectifier switch-node voltages. It can be observed that the poles of the step responses in each case are given by the roots of the same polynomial $f(s)$. Therefore, α_1, α_2, ω_1, and ω_2 are the same for all combinations of the inverter/rectifier switch-node voltages (indexed by y) and inverter output currents (indexed by x). The magnitude parameters I_{xy1} and I_{xy2} in (22) are obtained by evaluating the zeroes of the step responses of the inverter currents, as obtained by applying the above procedure. These parameters have different values depending on the combination of inverter/rectifier voltage and inverter output current being evaluated.

It is evident from (22)–(27) that the inverter output currents of the ICN converter can be expressed as a summation of time-shifted decaying sinusoidal functions. Utilizing the procedure described in Appendix A, the inverter output currents can be expressed in a closed form. For clarity, these expressions are split into steady-state and startup transient components. The expressions for the inverter output currents, as a response to the top and bottom inverter output voltages and the rectifier input voltage, $i_{x1}(t)$, $i_{x2}(t)$, and $i_{x3}(t)$, respectively, are given by

$$i_{x1}(t) = i_{x1s}(t) + i_{x1t}(t) \qquad (59)$$

$$i_{x2}(t) = i_{x2s}(t) + i_{x2t}(t) \qquad (60)$$

$$i_{x3}(t) = i_{x3s}(t) + i_{x3t}(t) \qquad (61)$$

where the steady-state and startup transient components of the two inverter output currents in response to the two inverter output voltages are given by (62)–(65) shown at the bottom of the next page. Here, $V_{1,\mathrm{ini}}$ and $V_{2,\mathrm{ini}}$ are the initial voltages at the two inverter switch nodes at time $t = 0$ (i.e., at the start of each burst cycle). For the inverter output currents in response to the rectifier input voltage, $i_{x3}(t)$ as expressed in (61), (x is 1 or 2), closed-form expressions for steady-state operation are given by (66) shown at the bottom of the next page. Here, T_r is the time lag of the rectifier, which is defined as the time instant $t'_K = T_r$ when the rectifier switches commutate, including the charging times of the parasitic capacitances, as discussed in Section V.

For startup transients, closed-form expressions for $i_{13}(t)$ and $i_{23}(t)$ are difficult to obtain, as an expression for the commutation time of the diode rectifier at the very beginning of the startup transient is difficult to determine. Hence, the actual commutation time is determined numerically by searching across the entire switching period, and utilizing the condition that the rectifier current is near zero at the commutation instant, taking into account that the actual commutation happens when the parasitic capacitances of the rectifier diodes are fully charged or discharged. It is worth mentioning that for an ICN converter utilizing an active rectifier (with transistors), the closed-form expressions for the transient components of $i_{13}(t)$ and $i_{23}(t)$ can also be obtained, and the resultant expressions are similar to those in (63) and (65).

Expressions for all the parameters used in (62)–(66) shown at the bottom of this page, listed as

$$I_{111} = V_{\mathrm{IN}}\beta_1\left[\left(\frac{1}{C_r N^2} + \frac{1}{C_{X2}}\right) - \omega_1^2\left(\frac{L_r}{N^2} + L_{X2}\right)\right] \tag{67}$$

$$I_{112} = V_{\mathrm{IN}}\beta_2\left[\left(\frac{1}{C_r N^2} + \frac{1}{C_{X2}}\right) - \omega_2^2\left(\frac{L_r}{N^2} + L_{X2}\right)\right] \tag{68}$$

$$I_{121} = -V_{\mathrm{IN}}\beta_1\left(\frac{1}{C_r N^2} - \omega_1^2\frac{L_r}{N^2}\right) \tag{69}$$

$$I_{122} = -V_{\mathrm{IN}}\beta_2\left(\frac{1}{C_r N^2} - \omega_2^2\frac{L_r}{N^2}\right) \tag{70}$$

$$I_{131} = -\left(\frac{V_{\mathrm{OUT}}}{N}\right)\beta_1\left(\frac{1}{C_{X2}} - \omega_1^2 L_{X2}\right) \tag{71}$$

$$I_{132} = -\left(\frac{V_{\mathrm{OUT}}}{N}\right)\beta_2\left(\frac{1}{C_{X2}} - \omega_2^2 L_{X2}\right) \tag{72}$$

$$I_{211} = -V_{\mathrm{IN}}\beta_1\left(\frac{1}{C_r N^2} - \omega_1^2\frac{L_r}{N^2}\right) \tag{73}$$

$$I_{212} = -V_{\mathrm{IN}}\beta_2\left(\frac{1}{C_r N^2} - \omega_2^2\frac{L_r}{N^2}\right) \tag{74}$$

$$I_{221} = V_{\mathrm{IN}}\beta_1\left[\left(\frac{1}{C_r N^2} + \frac{1}{C_{X1}}\right) - \omega_1^2\left(\frac{L_r}{N^2} + L_{X1}\right)\right] \tag{75}$$

$$I_{222} = V_{\mathrm{IN}}\beta_2\left[\left(\frac{1}{C_r N^2} + \frac{1}{C_{X1}}\right) - \omega_2^2\left(\frac{L_r}{N^2} + L_{X1}\right)\right] \tag{76}$$

$$I_{231} = -\left(\frac{V_{\mathrm{OUT}}}{N}\right)\beta_1\left(\frac{1}{C_{X1}} - \omega_1^2 L_{X1}\right) \tag{77}$$

$$I_{232} = -\left(\frac{V_{OUT}}{N}\right)\beta_2\left(\frac{1}{C_{X1}} - \omega_2^2 L_{X1}\right) \tag{78}$$

$$\beta_1 = \frac{1}{\omega_1\left(\omega_2^2 - \omega_1^2\right)\left(L_{X1}L_{X2} + L_{X1}\frac{L_r}{N^2} + L_{X2}\frac{L_r}{N^2}\right)} \tag{79}$$

$$\beta_2 = \frac{1}{\omega_2\left(\omega_1^2 - \omega_2^2\right)\left(L_{X1}L_{X2} + L_{X1}\frac{L_r}{N^2} + L_{X2}\frac{L_r}{N^2}\right)}. \tag{80}$$

$$i_{x1s}(t) = \begin{cases} \dfrac{I_{x11}\sin\left(\omega_1 t_K' - \frac{\omega_1 T_s}{4}\right)}{2\cos\left(\frac{\omega_1 T_s}{4}\right)} + \dfrac{I_{x12}\sin\left(\omega_2 t_K' - \frac{\omega_2 T_s}{4}\right)}{2\cos\left(\frac{\omega_2 T_s}{4}\right)}, & 0 \le t_K' < \frac{T_s}{2} \\ \dfrac{I_{x11}\sin\left(\frac{3\omega_1 T_s}{4} - \omega_1 t_K'\right)}{2\cos\left(\frac{\omega_1 T_s}{4}\right)} + \dfrac{I_{x12}\sin\left(\frac{3\omega_2 T_s}{4} - \omega_2 t_K'\right)}{2\cos\left(\frac{\omega_2 T_s}{4}\right)}, & \frac{T_s}{2} \le t_K' < T_s \end{cases} \tag{62}$$

$$\begin{aligned} i_{x1t}(t) = {} & \frac{V_{1,\mathrm{ini}}}{V_{\mathrm{IN}}} I_{x11} e^{-\alpha_1 t}\sin\omega_1 t + \frac{V_{1,\mathrm{ini}}}{V_{\mathrm{IN}}} I_{x12} e^{-\alpha_2 t}\sin\omega_2 t - \frac{I_{x11}}{2\cos\left(\frac{\omega_1 T_s}{4}\right)} e^{-(K-1)\alpha_1 T_s}\sin\left(-\omega_1 t_K' - K\omega_1 T_s + \frac{3\omega_1 T_s}{4}\right) \\ & - \frac{I_{x12}}{2\cos\left(\frac{\omega_2 T_s}{4}\right)} e^{-(K-1)\alpha_2 T_s}\sin\left(-\omega_2 t_K' - K\omega_2 T_s + \frac{3\omega_2 T_s}{4}\right) \end{aligned} \tag{63}$$

$$i_{x2s}(t) = \begin{cases} \frac{I_{x21}}{2\cos\left(\frac{\omega_1 T_s}{4}\right)}\sin\left(-\omega_1 t_K' - \frac{\omega_1 T_s}{4} + \omega_1\frac{\Delta}{\pi}T_s\right) + \frac{I_{x22}}{2\cos\left(\frac{\omega_2 T_s}{4}\right)}\sin\left(-\omega_2 t_K' - \frac{\omega_2 T_s}{4} + \omega_2\frac{\Delta}{\pi}T_s\right), & 0 \le t_K' < \frac{\Delta}{\pi}T_s \\ \frac{I_{x21}}{2\cos\left(\frac{\omega_1 T_s}{4}\right)}\sin\left(\omega_1 t_K' - \frac{\omega_1 T_s}{4} - \omega_1\frac{\Delta}{\pi}T_s\right) + \frac{I_{x22}}{2\cos\left(\frac{\omega_2 T_s}{4}\right)}\sin\left(\omega_2 t_K' - \frac{\omega_2 T_s}{4} - \omega_2\frac{\Delta}{\pi}T_s\right), & \frac{\Delta}{\pi}T_s \le t_K' < \frac{\Delta}{\pi}T_s + \frac{T_s}{2} \\ \frac{I_{x21}}{2\cos\left(\frac{\omega_1 T_s}{4}\right)}\sin\left(-\omega_1 t_K' + \frac{3\omega_1 T_s}{4} + \omega_1\frac{\Delta}{\pi}T_s\right) + \frac{I_{x22}}{2\cos\left(\frac{\omega_2 T_s}{4}\right)}\sin\left(-\omega_2 t_K' + \frac{3\omega_2 T_s}{4} + \omega_2\frac{\Delta}{\pi}T_s\right), & \frac{\Delta}{\pi}T_s + \frac{T_s}{2} \le t_K' < T_s \end{cases}, \tag{64}$$

$$\begin{aligned} i_{x2t}(t) = {} & \frac{V_{2,\mathrm{ini}}}{V_{\mathrm{IN}}} I_{x21} e^{-\alpha_1 t}\sin\omega_1 t + \frac{V_{2,\mathrm{ini}}}{V_{\mathrm{IN}}} I_{x22} e^{-\alpha_2 t}\sin\omega_2 t - \frac{I_{x21}}{2\cos\left(\frac{\omega_1 T_s}{4}\right)} e^{-(K-1)\alpha_1 T_s}\sin\left(-\omega_1 t_K' - K\omega_1 T_s + \frac{3\omega_1 T_s}{4}\right) \\ & - \frac{I_{x22}}{2\cos\left(\frac{\omega_2 T_s}{4}\right)} e^{-(K-1)\alpha_2 T_s}\sin\left(-\omega_2 t_K' - K\omega_2 T_s + \frac{3\omega_2 T_s}{4}\right) \end{aligned} \tag{65}$$

$$i_{x3s}(t) = \begin{cases} \frac{I_{x31}}{2\cos\left(\frac{\omega_1 T_s}{4}\right)}\sin\left(-\omega_1 t_K' - \frac{\omega_1 T_s}{4} + \omega_1 T_r\right) + \frac{I_{x32}}{2\cos\left(\frac{\omega_2 T_s}{4}\right)}\sin\left(-\omega_2 t_K' - \frac{\omega_2 T_s}{4} + \omega_2 T_r\right), & 0 \le t_K' < T_r \\ \frac{I_{x31}}{2\cos\left(\frac{\omega_1 T_s}{4}\right)}\sin\left(\omega_1 t_K' - \frac{\omega_1 T_s}{4} - \omega_1 T_r\right) + \frac{I_{x32}}{2\cos\left(\frac{\omega_2 T_s}{4}\right)}\sin\left(\omega_2 t_K' - \frac{\omega_2 T_s}{4} - \omega_2 T_r\right), & T_r \le t_K' < T_r + \frac{T_s}{2} \\ \frac{I_{x31}}{2\cos\left(\frac{\omega_1 T_s}{4}\right)}\sin\left(-\omega_1 t_K' + \frac{3\omega_1 T_s}{4} + \omega_1 T_r\right) + \frac{I_{x32}}{2\cos\left(\frac{\omega_2 T_s}{4}\right)}\sin\left(-\omega_2 t_K' + \frac{3\omega_2 T_s}{4} + \omega_2 T_r\right), & T_r + \frac{T_s}{2} \le t_K' < T_s \end{cases}. \tag{66}$$

REFERENCES

[1] R. L. Steigerwald, "A comparison of half-bridge resonant converter topologies," *IEEE Trans. Power Electron.*, vol. 3, no. 2, pp. 174–182, Apr. 1988.

[2] G. Ivensky, A. Kats, and S. Ben-Yaakov, "An RC load model of parallel and series-parallel resonant DC-DC converters with capacitive output filter," *IEEE Trans. Power Electron.*, vol. 14, no. 3, pp. 515–521, May 1999.

[3] J. G. Hayes and M. G. Egan, "Rectifier-compensated fundamental mode approximation analysis of the series parallel LCLC family of resonant converters with capacitive output filter and voltage-source load," in *Proc. IEEE Power Electron. Spec. Conf.*, Charleston, SC, USA, Jul. 1999, pp. 1030–1036.

[4] A. K. S. Bhat, "A generalized steady-state analysis of resonant converters using two-port model and Fourier-series approach," *IEEE Trans. Power Electron.*, vol. 13, no. 1, pp. 142–151, Jan. 1998.

[5] T. J. Aprille and T. N. Trick, "Steady-state analysis of nonlinear circuits with periodic inputs," *Proc. IEEE*, vol. 60, no. 1, pp. 108–114, Jan. 1972.

[6] R. L. Steigerwald, "High-frequency resonant transistor DC-DC converters," *IEEE Trans. Ind. Electron.*, vol. 31, no. 2, pp. 181–191, May 1984.

[7] H. R. Visser and P. P. J. van den Bosch, "Modeling of periodically switching networks," in *Proc. IEEE Power Electron. Spec. Conf.*, Cambridge, MA, USA, Jun. 1991, pp. 67–73.

[8] O. P. Mandhana and R. G. Hoft, "Steady state analysis of DC to DC resonant converter," in *Proc. IEEE Appl. Power Electron. Conf.*, Dallas, TX, USA, Mar. 1991, pp. 580–586.

[9] D. V. Malyna, J. L. Duarte, M. A. M. Hendrix, and F. B. M. van Horck, "A comparison of methods for finding steady-state solution in power electronic circuits," in *Proc. Int. Power Electron. Motion Contr. Conf.*, Xi'an, China, Aug. 2004, pp. 1700–1705.

[10] R. Yu, G. K. Y. Ho, B. M. H. Pong, B. W. K. Ling, and J. Lam, "Computer-aided design and optimization of high-efficiency LLC series resonant converter," *IEEE Trans. Power Electron.*, vol. 27, no. 7, pp. 3243–3256, Jul. 2012.

[11] P. C. K. Luk, S. Aldhaher, W. Fei, and J. F. Whidborne, "State-space modeling of a class E2 converter for inductive links," *IEEE Trans. Power Electron.*, vol. 30, no. 6, pp. 3242–3251, Jun. 2015.

[12] A. Kumar, J. Lu, and K. K. Afridi, "Enhanced-accuracy augmented state-space approach to steady-state modeling of resonant converters," in *Proc. IEEE Workshop Contr. Model. Power Electron.*, Vancouver, Canada, Jul. 2015, pp. 1–6.

[13] F. C. Y. Lee and T. G. Wilson, "Nonlinear analysis of a family of LC tuned inverters," in *Proc. IEEE Power Electron. Spec. Conf.*, Murray Hill, NJ, USA, Jun. 1974, pp. 223–232.

[14] W. W. Burns and T. G. Wilson, "State trajectories used to observe and control DC-to-DC converters," *IEEE Trans. Aerosp. Electron. Syst.*, vol. 12, no. 6, pp. 706–717, Nov. 1976.

[15] V. Vorperian and S. Cuk, "A complete DC analysis of the series resonant converter," in *Proc. IEEE Power Electron. Spec. Conf.*, Cambridge, MA, USA, Jun. 1982, pp. 85–100.

[16] R. Oruganti and F. C. Lee, "Resonant power processors, Part I—State plane analysis," *IEEE Trans. Ind. Appl.*, vol. 21, no. 6, pp. 1453–1460, Nov. 1985.

[17] A. F. Wittulski and R. W. Erickson, "Steady-state analysis of the series resonant converter," *IEEE Trans. Aerosp. Electron. Syst.*, vol. 21, no. 6, pp. 791–799, Nov. 1985.

[18] C. Q. Lee and K. Siri, "Analysis and design of series resonant converter by state-plane diagram," *IEEE Trans. Aerosp. Electron. Syst.*, vol. 22, no. 6, pp. 757–763, Nov. 1986.

[19] S. G. Trabert and R. W. Erickson, "Steady state analysis of the duty cycle controlled series resonant converter," in *Proc. IEEE Power Electron. Spec. Conf.*, Blacksburg, VA, USA, Jun. 1987, pp. 545–556.

[20] I. Batarseh and C. Q. Lee, "State-plane analysis of high order parallel resonant converters," in *Proc. Midwest Symp. Circuits Syst.*, Monterey, CA, USA, May 1992, pp. 939–942.

[21] W. Feng, F. C. Lee, and P. Mattavelli, "Optimal trajectory control of burst mode for LLC resonant converter," *IEEE Trans. Power Electron.*, vol. 28, no. 1, pp. 457–466, Jan. 2013.

[22] F. M. Ibanez, J. M. Echeverria, J. Vadillo, and L. Fontan, "State-plane analysis of anomalous step-up behavior in series-resonant converters," *IEEE J. Emerg. Sel. Topics Power Electron.*, vol. 4, no. 3, pp. 1026–1035, Sep. 2016.

[23] I. Batarseh and C. Q. Lee, "Steady-state analysis of the parallel resonant converter with LLCC-type commutation network," *IEEE Trans. Power Electron.*, vol. 6, no. 3, pp. 525–538, Jul. 1991.

[24] I. Batarseh, "Resonant converter topologies with three and four energy storage elements," *IEEE Trans. Power Electron.*, vol. 9, no. 1, pp. 64–73, Jan. 1994.

[25] J. G. Hayes, M. G. Egan, J. M. D. Murphy, S. E. Schulz, and J. T. Hall, "Wide-load-range resonant converter supplying the SAE J-1773 electric vehicle inductive charging interface," *IEEE Trans. Ind. Appl.*, vol. 35, no. 4, pp. 884–895, Jul. 1999.

[26] M. Borage, K. V. Nagesh, M. S. Bhatia, and S. Tiwari, "Resonant immittance converter topologies," *IEEE Trans. Ind. Electron.*, vol. 58, no. 3, pp. 971–978, Mar. 2011.

[27] D. Huang, F. C. Lee, and D. Fu, "Classification and selection methodology for multi-element resonant converters," in *Proc. IEEE Appl. Power Electron. Conf. Expo.*, Fort Worth, TX, USA, Mar. 2011, pp. 558–565.

[28] N. Shafiei, M. Pahlevaninezhad, H. Farzanehfard, A. Bakhshai, and P. Jain, "Analysis of a fifth-order resonant converter for high-voltage DC power supplies," *IEEE Trans. Power Electron.*, vol. 28, no. 1, pp. 85–100, Jan. 2013.

[29] W. Inam, K. K. Afridi, and D. J. Perreault, "High efficiency resonant DC/DC converter utilizing a resistance compression network," *IEEE Trans. Power Electron.*, vol. 29, no. 8, pp. 4126–4135, Aug. 2014.

[30] D. Thenathayalan, C. G. Lee, and J. H. Park, "High-order resonant converter topology with extremely low-coupling contactless transformers," *IEEE Trans. Power Electron.*, vol. 31, no. 3, pp. 2347–2361, Mar. 2016.

[31] J. Lu, D. J. Perreault, D. M. Otten, and K. K. Afridi, "Impedance control network resonant DC-DC converter for wide-range high-efficiency operation," *IEEE Trans. Power Electron.*, vol. 31, no. 7, pp. 5040–5056, Jul. 2016.

[32] J. Lu and K. K. Afridi, "High efficiency impedance control network resonant DC-DC converter with optimized startup control," *IEEE Trans. Ind. Appl.*, vol. 53, no. 4, pp. 3880–3889, Jul./Aug. 2017.

[33] S. J. Gunter, K. K. Afridi, D. M. Otten, R. Abramson, and D. J. Perreault, "Impedance control network resonant step-down DC-DC converter architecture," in *Proc. IEEE Energy Convers. Congr. Expo.*, Montreal, Canada, Sep. 2015, pp. 539–547.

[34] A. Kumar and K. K. Afridi, "Megahertz-frequency isolated resonant dc-dc converter using impedance control network for high-efficiency wide-range operation," in *Proc. IEEE Energy Convers. Congr. Expo.*, Montreal, Canada, Sep. 2015, pp. 5081–5088.

[35] Y. Liu, A. Kumar, J. Lu, D. Maksimovic, and K. K. Afridi, "New design methodology for megahertz-frequency resonant dc-dc converters using impedance control network architecture," in *Proc. IEEE Appl. Power Electron. Conf. Expo.*, Long Beach, CA, USA, Mar. 2016, pp. 1392–1397.

[36] A. Kumar, J. Lu, and K. K. Afridi, "Power density and efficiency enhancement in impedance control network resonant DC-DC converters using topology morphing control," in *Proc. IEEE Workshop Contr. Model. Power Electron.*, Trondheim, Norway, Jun. 2016, pp. 1–6.

[37] J. Lu, A. Kumar, and K. K. Afridi, "Step-down impedance control network resonant DC-DC converter utilizing an enhanced phase-shift control for wide-input-range operation," in *Proc. IEEE Energy Convers. Congr. Expo.*, Milwaukee, WI, USA, Sep. 2016, pp. 1–6.

[38] A. Kumar, J. Lu, S. Pervaiz, A. Sepahvand, and K. K. Afridi, "High power density impedance control network DC-DC converter utilizing an integrated magnetic structure," in *Proc. IEEE Energy Convers. Congr. Expo.*, Milwaukee, WI, USA, Sep. 2016, pp. 1–6.

[39] J. Lu, A. Kumar, and K. K. Afridi, "A step-superposition based analysis approach to modeling resonant converters," in *Proc. IEEE Workshop Contr. Model. Power Electron.*, Vancouver, Canada, Jul. 2015, pp. 1–7.

[40] R. W. Erickson and D. Maksimovic, *Fundamentals of Power Electronics*, 2nd ed. New York, NY, USA: Springer, 2001.

[41] N. O. Sokal and A. D. Sokal, "Class E—A new class of high-efficiency tuned single-ended switching power amplifiers," *IEEE J. Solid-State Circuits*, vol. 10, no. 3, pp. 168–176, Jun. 1975.

[42] F. H. Raab, "Class-F power amplifiers with maximally flat waveforms," *IEEE Trans. Microw. Theory Techn.*, vol. 45, no. 11, pp. 2007–2012, Nov. 1997.

[43] S. D. Kee, I. Aoki, A. Hajimiri, and D. Rutledge, "The class-E/F family of ZVS switching amplifiers," *IEEE Trans. Microw. Theory Techn.*, vol. 51, no. 6, pp. 1677–1690, Jun. 2003.

[44] Z. Kaczmarczyk, "High-efficiency class E, EF2, and E/F3 inverters," *IEEE Trans. Ind. Electron.*, vol. 53, no. 5, pp. 1584–1593, Oct. 2006.

[45] J. M. Rivas, Y. Han, O. Leitermann, A. D. Sagneri, and D. J. Perreault, "A high-frequency resonant inverter topology with low-voltage stress," *IEEE Trans. Power Electron.*, vol. 23, no. 4, pp. 1759–1771, Jul. 2008.

Jie Lu (S'14–M'17) received the B.Eng. degree in automation from Harbin Institute of Technology, Harbin, China, in 2012, and the M.S. and Ph.D. degrees in electrical engineering from the University of Colorado-Boulder (CU Boulder), Boulder, CO, USA, in 2015 and 2016, respectively. Since August 2016, he has been a senior power electronics design engineer at FINsix Corporation, Menlo Park, CA, USA.

His research interests include high-frequency high-power-density dc-dc, ac-dc and dc-ac converters, modeling and control of power electronics, and application of these in consumer and automotive electronics.

Dr. Lu received the First Prize Paper Award from the IEEE Industry Applications Society Renewable and Sustainable Energy Conversion Systems Committee in 2016, the Gold Research Award from CU Boulder in 2016, and an Outstanding Presentation Award from IEEE Applied Power Electronics Conference in 2015.

Ashish Kumar (S'15) received the B.Tech. degree in electrical engineering from Indian Institute of Technology Delhi, Delhi, India, in 2011, and the M.S. degree in electrical engineering from the University of Colorado Boulder, Boulder, CO, USA, in 2016, where he is currently working toward the Ph.D. degree in electrical engineering.

His research interests include modeling, design, and optimization of high-performance resonant converters.

Mr. Kumar received the First Prize Award in the Student Demonstration Competition at the IEEE ECCE in 2016, the Platinum Research Award from CU Boulder in 2016, and the Silver Research Award from CU Boulder in 2017, and is the coauthor of two Best Paper Award winning papers, one each at the IEEE COMPEL in 2016 and the COMPEL in 2017.

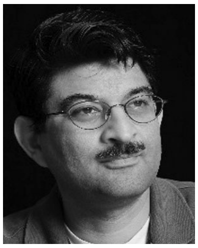

Khurram K. Afridi (S'93–M'98–SM'16) received the B.S. degree in electrical engineering from California Institute of Technology (Caltech), Pasadena, CA, USA, in 1989, and the S.M. and Ph.D. degrees in electrical engineering and computer science from Massachusetts Institute of Technology (MIT), Cambridge, MA, USA, in 1992 and 1998, respectively.

During summers and between degrees, he was with JPL, with Lutron, with Philips, and with Schlumberger. In 1997, he joined the founding team of Techlogix as the Chief Technology Officer and became the Chief Operating Officer in 2000. From 2004 to 2008, he also led the development of LUMS School of Science and Engineering as the Project Director, and was appointed as an Associate Professor and the Werner-von-Siemens Chair for Power Electronics in 2008. From 2009 to 2014, he was a Visiting Associate Professor in the Department of Electrical Engineering and Computer Science, MIT. Since January 2014, he has been an Assistant Professor in the Department of Electrical, Computer and Energy Engineering, University of Colorado (CU) Boulder, Boulder, CO, USA. His research interests include power electronics and energy systems incorporating power electronic controls.

Dr. Afridi is an Associate Editor of the IEEE TRANSACTIONS ON TRANSPORTATION ELECTRIFICATION. He received Caltech's Carnation Merit Award, CU Boulder's Goh Faculty Fellowship, the BMW Scientific Award, and the NSF CAREER Award. He is the coauthor of four IEEE prize papers.